Calhoun
Institutional Archive of the Naval Postgraduate School

Calhoun: The NPS Institutional Archive

Theses and Dissertations | Thesis Collection

2001-12

Maritime frontogenesis.

McDougall, Catherine M.

http://hdl.handle.net/10945/9711

NAVAL POSTGRADUATE SCHOOL
Monterey, California

THESIS

MARITIME FRONTOGENESIS

by

Catherine M. McDougall

December 2001

Thesis Advisor:	R. T. Williams
Second Reader:	D. K. Miller

Approved for public release; distribution is unlimited.

THIS PAGE INTENTIONALLY LEFT BLANK

REPORT DOCUMENTATION PAGE		*Form Approved OMB No. 0704-0188*

1. AGENCY USE ONLY *(Leave blank)*	2. REPORT DATE December 2001.	3. REPORT TYPE AND DATES COVERED Master's Thesis	
4. TITLE AND SUBTITLE: Maritime Frontogenesis		**5. FUNDING NUMBERS**	
6. AUTHOR(S) McDougall, Catherine M.			
7. PERFORMING ORGANIZATION NAME(S) AND ADDRESS(ES) Naval Postgraduate School Monterey, CA 93943-5000		**8. PERFORMING ORGANIZATION REPORT NUMBER**	
9. SPONSORING /MONITORING AGENCY NAME(S) AND ADDRESS(ES) N/A		**10. SPONSORING/MONITORING AGENCY REPORT NUMBER**	

11. SUPPLEMENTARY NOTES The views expressed in this thesis are those of the author and do not reflect the official policy or position of the Department of Defense or the U.S. Government.

12a. DISTRIBUTION / AVAILABILITY STATEMENT Approved for public release; distribution unlimited	12b. DISTRIBUTION CODE

13. ABSTRACT *(maximum 200 words)*

Numerical experiments are conducted with a hydrostatic primitive equation model initialized in a baroclinically unstable state to simulate the passage of cold fronts over the ocean. The model includes K-theory planetary boundary layer (PBL) parameterization with implicitly defined diffusion coefficients. An adiabatic and inviscid simulation provided the control for these experiments. The PBL simulations are integrated 1) with z_o held constant at 0.4 m and no heat flux; 2) with sea surface temperature (SST) set equal to θ_1 at t = 0 h; 3) with a 5° warmer SST; 4) with diffusion coefficients set equal to 1. Horizontal resolution is increased to achieve smaller scale fronts in the inviscid and ocean simulations. The frontogenetic effects of shear, tilting, convergence, and the PBL on isentropic surfaces are evaluated.

Relative to the inviscid simulation, the PBL simulations produce reduced frontogenesis. Surface heat and momentum fluxes combined with turbulent mixing of heat promote the development of a deep, well-mixed layer whose depth is dependent on the air-sea temperature difference. The rate of frontogenesis is extremely dependent on the parameterization of the PBL, specifically surface roughness lengths. Smaller scale fronts were produced during the ocean simulations than the PBL land case. Forcing in all simulations is due primarily to shearing deformation initially. As the wave grows in amplitude, convergence contributes more to frontogenesis than shear. Other terms in the frontogenetic equation become important in the PBL simulations.

14. SUBJECT TERMS frontogenesis, numerical simulation, boundary layer, K closure			15. NUMBER OF PAGES 61
			16. PRICE CODE
17. SECURITY CLASSIFICATION OF REPORT Unclassified	18. SECURITY CLASSIFICATION OF THIS PAGE Unclassified	19. SECURITY CLASSIFICATION OF ABSTRACT Unclassified	20. LIMITATION OF ABSTRACT UL

THIS PAGE INTENTIONALLY LEFT BLANK

MARITIME FRONTOGENESIS

Catherine M. McDougall
Lieutenant Commander, United States Navy
B. S., University of Michigan, 1992

Submitted in partial fulfillment of the
requirements for the degree of

**MASTER OF SCIENCE IN METEOROLOGY AND PHYSICAL
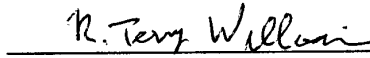OCEANOGRAPHY**

from the

**NAVAL POSTGRADUATE SCHOOL
December 2001**

Author: _____
Catherine M. McDougall

Approved by: _____
R. Terry Williams, Thesis Advisor

_____
Douglas K Miller, Second Reader

_____
Carlyle H. Wash, Chairman
Department of Meteorology

iii

THIS PAGE INTENTIONALLY LEFT BLANK

ABSTRACT

Numerical experiments are conducted with a hydrostatic primitive equation model initialized in a baroclinically unstable state to simulate the passage of cold fronts over the ocean. The model includes K-theory planetary boundary layer (PBL) parameterization with implicitly defined diffusion coefficients. An adiabatic and inviscid simulation provided the control for these experiments. The PBL simulations are integrated 1) with z_o held constant at 0.4 m and no heat flux; 2) with sea surface temperature (SST) set equal to θ_1 at t = 0 h; 3) with a 5° warmer SST; 4) with diffusion coefficients set equal to 1. Horizontal resolution is increased to achieve smaller scale fronts in the inviscid and ocean simulations. The frontogenetic effects of shear, tilting, convergence, and the PBL on isentropic surfaces are evaluated.

Relative to the inviscid simulation, the PBL simulations produce reduced frontogenesis. Surface heat and momentum fluxes combined with turbulent mixing of heat promote the development of a deep, well-mixed layer whose depth is dependent on the air-sea temperature difference. The rate of frontogenesis is extremely dependent on the parameterization of the PBL, specifically surface roughness lengths. Smaller scale fronts were produced during the ocean simulations than the PBL land case. Forcing in all simulations is due primarily to shearing deformation initially. As the wave grows in amplitude, convergence contributes more to frontogenesis than shear. Other terms in the frontogenetic equation become important in the PBL simulations.

THIS PAGE INTENTIONALLY LEFT BLANK

TABLE OF CONTENTS

THIS PAGE INTENTIONALLY LEFT BLANK

LIST OF FIGURES

LIST OF TABLES

THIS PAGE INTENTIONALLY LEFT BLANK

I. INTRODUCTION

The effect of the boundary layer on the development and modification of fronts as they move over various surface conditions is not well understood. Specifically, the interaction of fronts with the ocean has been a standing problem to both synoptic and dynamic meteorologists. Because the ocean is an infinite source of energy for the atmosphere, fronts over the ocean are very sensitive to the temperature differences between the air and the sea. For example, when the air is much colder than the water, there will be a large heat flux into the atmosphere with strong mixing. A deep mixed layer is expected behind a cold front where the air is generally colder than the water. This described frontal structure is very similar to that observed by Fleagle *et al.* (1988). They found very large vertical velocities and frontal scales down to a few kilometers. When the air is warmer than the water, very stable conditions with much less vertical mixing are expected.

Boundary layer processes have a significant influence on surface fronts because they have the largest gradients at the surface in the absence of turbulent diffusion. Williams (1974) produced steady state fronts using simple parameterizations of the horizontal and vertical turbulent diffusion of momentum and heat. More realistic frontal structure was obtained by Keyser and Anthes (1982) who simulated Eady wave frontogenesis with a boundary layer representation. The major features in their results include a narrow updraft at the top of the boundary layer at the warm edge of the front, a stable layer capping the boundary layer to the rear of the frontal zone, and a slightly unstable or neutral lapse rate in the boundary layer behind the front.

Thompson and Williams (1997) used a hydrostatic primitive equation model with both K-theory and second-order closure scheme simulations to study maritime frontogenesis. In order to identify the boundary layer processes important to maritime frontogenesis, moist processes were not included. The results indicated that strong warm and cold fronts formed in the adiabatic and inviscid case, but the vertical motion fields were comparatively weak. In both the K-theory and second-order closure scheme simulations, the boundary layer in the cold air was highly unstable and deep mixed layers

formed with a large generation of turbulence. The largest cross-front temperature gradients existed in the frontal zone above the mixed layer. These structures were in qualitative agreement with observations of maritime cold fronts over the northwest Pacific Ocean. However, the simulated fronts did not have the small spatial scales that were observed by Fleagle *et al.* (1988).

The boundary layer response to changes in sea surface temperature of a frontal case over the Atlantic Ocean in FASTEX was predicted by Thompson *et al.* (2000) using the U.S. Navy Coupled Ocean-Atmospheric Mesoscale Prediction System (COAMPS) model (Hodur 1997). Initially the front was over colder water and a very shallow mixed layer developed in the cold air. The boundary layer was very stable. The front then passed over much warmer water and a deep convective boundary layer rapidly developed. The increased vertical mixing damped the intense low-level jet on the warm side of the front.

This study investigates the structure of fronts that form over the ocean and the boundary layer influence on those fronts passing over the ocean. The basic model is the two-dimension primitive equation model employed by Williams *et al.* (1992) with a first order K-theory boundary layer parameterization following Keyser and Anthes (1982). Fronts will be forced in this study with a shearing wind field operating on a horizontal temperature gradient. Following Thompson and Williams (1997) condensation effects will be neglected. Williams *et al.* (1981) found that condensation did not have a strong influence on surface fronts. The secondary goal is to determine frontal structures as a function of the air-sea temperature difference. Fleagle *et al.* (1988) and Chien *et al.* (2001) have observed cold fronts over the northern Pacific with frontal scales as low as 1-5 km. These fronts had very little vertical tilt and there was intense mixing in the cold air behind the front. Thompson and Williams (1997) were able to simulate this basic frontal structure, but could not simulate the small scales because the three dimensional model had a grid size of 40 km.

The simulations are run for both inviscid and planetary boundary layer (PBL) modes. The basic model and PBL formulations are developed in Chapter II. Frontogenetic forcing terms used to quantify causes of frontogenesis and frontolysis are

developed in Chapter III. Numerical solutions are presented and discussed in Chapter IV, and the results are summarized in Chapter V.

THIS PAGE INTENTIONALLY LEFT BLANK

II.   MODEL DESCRIPTION

This study uses a two-dimensional hydrostatic primitive equation model, whose equations are solved numerically using finite differencing on an Arakawa B grid (Arakawa and Lamb 1977). Because the vertical scales are much smaller than the horizontal resolution, the hydrostatic equation model is used. Finite differences are centered in time and space, with an Euler backward time step inserted every fourth iteration to control solution separation. Convective adjustment is applied every time step by vertically averaging the potential temperature field in areas of static instability. The convective adjustment perhaps could be applied less frequently. In the model the time dependent quantities are functions of x and z only. The model domain extends 4000 km in the east-west (x) direction and 9 km vertically. The horizontal grid spacing varies and there are 50 uniformly spaced vertical levels in z. The upper boundary is a rigid lid and the horizontal boundaries are periodic. The time step varies depending on horizontal grid spacing.

A.   BASIC EQUATIONS

The equations developed here, following Williams *et al.* (1992) are adapted to flat topography. The vertical axis is normalized with the height of the upper boundary, H, and follows

$$\sigma = \frac{z}{H} \tag{1}$$

The lower boundary is at $\sigma = 0$ and the upper boundary is at $\sigma = 1$. The Boussinesq equations (Ogura and Philips 1962) are transformed with equation (1) to give

$$\frac{\partial \mathbf{V}}{\partial t} + \mathbf{V} \bullet \nabla \mathbf{V} + \dot{\sigma} \frac{\partial \mathbf{V}}{\partial \sigma} = -\nabla \phi - f\mathbf{k} \times \mathbf{V} + \mathbf{F} \tag{2}$$

$$\frac{\partial \theta}{\partial t} + \mathbf{V} \bullet \nabla \theta + \dot{\sigma} \frac{\partial \theta}{\partial \sigma} = \mathbf{Q} \tag{3}$$

$$\nabla \bullet \mathbf{V} + \frac{\partial \dot{\sigma}}{\partial \sigma} = 0 \tag{4}$$

$$\frac{\partial \phi}{\partial \sigma} = \frac{g}{\theta_o} H\theta \tag{5}$$

where

$$\theta = T\left(\frac{p_o}{p}\right)^{\kappa} - \theta_o$$

$$\phi = [c_p \frac{p_o}{p}^{\kappa} + \frac{gz}{\theta_o} - c_p]$$

F and **Q** are fourth order diffusion terms for momentum and potential temperature plus the required boundary layer terms.

B.   INITIAL AND BOUNDARY CONDITIONS

The frontogenesis simulations are initialized with a small amplitude temperature perturbation. The basic state consisting of a 37 m s^{-1} westerly jet at the upper boundary decreasing (linearly in z) to 2 m s^{-1} at the surface and an initial temperature field with a constant static stability and a small perturbation which is independent of z:

$$\theta(x,z,0) = \frac{\partial \overline{\theta_I}}{\partial z}(z - \frac{H}{2}) - A\cos(\frac{2\pi x}{L} - B) \tag{6}$$

The v component of the wind is zero to start. The initial temperature perturbation has a wavelength equal to the model's horizontal domain, L. Given such a baroclinically unstable initial state, rapid frontogenesis may be anticipated. Figure 1 gives the initial u and theta fields for all model runs. Constants are contained in Table 1.

For all but one experiment, the sea surface temperature is set equal to the air temperature at the lowest model level at the initial time. It is fixed at this value for the duration of the model run. For one run, the sea surface temperature is set to 287 K which is approximately 5 degrees warmer than the other simulations.
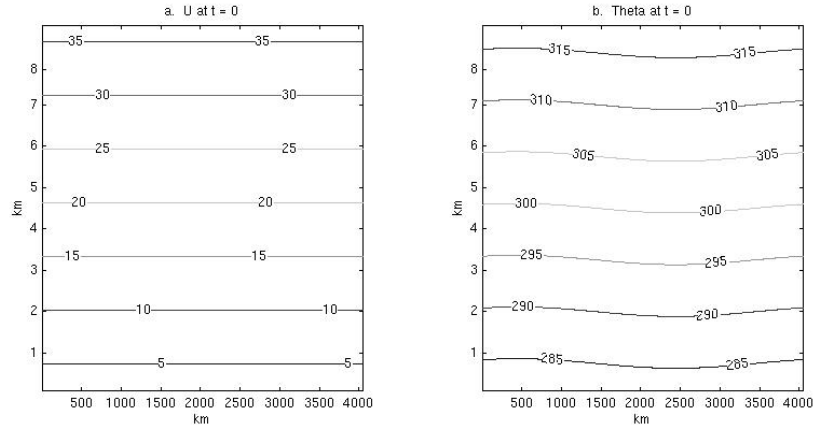
Figure 1.   Initial fields: (a) cross-front velocity (m s^{-1}); (b) potential temperature (K).

Parameter	Numerical value
L	4000 km
H	9 km
Δx	10 km or 5 km
$\Delta \sigma$	1/50
Δt	30 sec for Δx = 10 km
	10 sec for Δx = 5 km
$\partial \overline{\theta}_i/\partial z$	3.9 K km^{-1}
A	1.44/π
B	-1.78π
C	0.06
Ri$_c$	1.0
κ	0.4
λ_m	150 m
λ_h	350 m
K$_{z0}$	1.0
R	0.74
f	10^{-4} s^{-1}
g	9.8 m s^{-1}
c$_p$	1003 m^2 s^{-2} K^{-1}
θ_o	300 K
p$_o$	1000 mb

Table 1.   Specification of constant parameters.

C.   BOUNDARY LAYER PARAMETERAZION

1.   Surface Fluxes

The lower boundary conditions are relatively simple since cases are run over the ocean. The parameterization scheme for the surface fluxes is based on Monin-Obukhov (1954) similarity theory which gives

$$\overline{u'w'} = -\frac{uu_*^2}{\sqrt{u^2+v^2}} \tag{7}$$

$$\overline{v'w'} = -\frac{vu_*^2}{\sqrt{u^2+v^2}} \tag{8}$$

$$\overline{w'\theta'} = -\kappa u_* \theta_* \tag{9}$$

where

$$u_* = \frac{\kappa\sqrt{u^2+v^2}}{\ln\left(\dfrac{z}{z_o}\right)-\psi_m} \tag{10}$$

$$\theta_* = \frac{\kappa(\theta_1 - \theta_{sea})}{\ln\left(\dfrac{z}{z_{oh}}\right)-\psi_h} \tag{11}$$

Here z_o is the surface roughness length, z_{oh} is the surface roughness length for heat, ψ_m is the surface layer stability correction function for momentum and ψ_h is the surface layer stability correction function for heat. The roughness length is calculated using

$$z_o = \frac{z}{\exp(\frac{\kappa^2}{C_{DN}})^{\frac{-1}{2}}} \tag{12}$$

C_{DN} is the drag coefficient for momentum in neutral conditions and κ is the von Karmen constant. The ratio of the drag coefficients for momentum and heat, R, was estimated by Businger *et al.* (1971) and is used to calculate z_{oh}. Initial u_* and θ_* are calculated using

$$u_* = \frac{\kappa\sqrt{u^2 + v^2}}{\ln\left(\dfrac{z}{z_o}\right)} \tag{13}$$

$$\theta_* = \frac{\kappa(\theta_1 - \theta_{sea})}{\ln\left(\dfrac{z}{z_{oh}}\right)} \tag{14}$$

In equation (12), the neutral drag coefficient, C_{DN}, is computed from V_1 using an algebraic expression (Garrett 1977, 1992)

$$C_{DN} = (0.75 + 0.067V_1) \times 10^{-3} \quad V_1 < 20 \text{ m s}^{-1} \tag{15}$$

$$C_{DN} = (0.775 + 0.066V_1) \times 10^{-3} \quad V_1 > 20 \text{ m s}^{-1} \tag{16}$$

where V_1 is the wind speed at the 1st level of the model.

Following Monin-Obovkov (1954) similarity theory, the scaling length, L, which characterizes the bouyancy in the surface layer is computed

$$L = \frac{u_*^2 \bar{\theta}}{\kappa g \theta_*} \tag{17}$$

where $\bar{\theta}$ is the average potential temperature at the first level of the model. Given the gradient profile functions

$$\Phi_m(\frac{z}{L}) = \frac{\kappa z}{u_*}\frac{\partial u}{\partial z} \tag{18}$$

$$\Phi_h(\frac{z}{L}) = \frac{\kappa z}{\theta_*}\frac{\partial \theta}{\partial z} \tag{19}$$

ψ_h and ψ_m can be determined through integration. The dimensionless similarity gradient functions, Φ_m and Φ_h, have been deduced from observations.

In unstable conditions ($z/L < 0$), the Dyer (1974) and Hicks (1970) formulations are used

$$\Phi_m(\frac{z}{L}) = (1 - 16\frac{z}{L})^{\frac{-1}{4}} \tag{20}$$

9

$$\Phi_h\left(\frac{z}{L}\right) = \left(1 - 16\frac{z}{L}\right)^{\frac{-1}{2}} \tag{21}$$

and ψ_h and ψ_m are taken from Paulson (1970)

$$\psi_m\left(\frac{z}{L}\right) = \frac{\Pi}{2} - 2a\tan(y) + \log\frac{(1+y)^2(1+y^2)}{8} \tag{22}$$

$$\psi_h\left(\frac{z}{L}\right) = 2\log\left\{\frac{(1+y^2)}{2}\right\} \tag{23}$$

with $y = \left(1 - 16\frac{z}{L}\right)^{\frac{1}{4}}$.

In stable conditions ($z/L > 0$), Φ_m has the form indicated by Högstrom (1988)

$$\Phi_m\left(\frac{z}{L}\right) = 1 + 5\frac{z}{L} \tag{24}$$

and Φ_h is determined through the Ellison and Turner (1959) relationship for the ratio $\frac{\Phi_m}{\Phi_h}$

$$\Phi_h\left(\frac{z}{L}\right) = \left(1 + 4\frac{z}{L}\right)^2 \tag{25}$$

ψ_h and ψ_m are taken from Holtslag and De Bruin (1988)

$$\psi_m\left(\frac{z}{L}\right) = -\frac{2}{3}b\left(\frac{z}{L} - \frac{5}{0.35}\right)e^{-0.35\frac{z}{L}} - \frac{z}{L} - \frac{(5)(\frac{2}{3})}{0.35} \tag{26}$$

$$\psi_h\left(\frac{z}{L}\right) = -\frac{2}{3}\left(\frac{z}{L} - \frac{5}{0.35}\right)e^{-0.35\frac{z}{L}} - \left(1 + \frac{2}{3}\frac{z}{L}\right)^{1.5} - \frac{(5)(\frac{2}{3})}{0.35} + 1 \tag{27}$$

2.   K-Theory Boundary Layer Parameterization

The boundary layer parameterization follows the approach used by Keyser and Anthes (1982) which is based on the planetary boundary layer parameterization of Blackadar (1979). Turbulent fluxes are represented in K theory by

$$\overline{u'w'} = -K_m \frac{\partial u}{\partial z} \tag{28}$$

$$\overline{v'w'} = -K_m \frac{\partial v}{\partial z} \tag{29}$$

$$\overline{\theta'w'} = -K_h \frac{\partial \theta}{\partial z} \tag{30}$$

The boundary layer diffusion coefficients K_m and K_h are calculated implicitly from model shear and stability fields. The equations are solved in terms of the mixing length, l, vertical shear $\left|\frac{\partial V}{\partial z}\right|$, and the Richardson number, given by

$$Ri = \frac{\dfrac{g}{\theta_o} \dfrac{\partial \theta}{\partial z}}{\left|\dfrac{\partial V}{\partial z}\right|^2} \tag{31}$$

Much debate has been given to what l should be. Keyser and Anthes use a constant value of l = 100 m while most others (Mellor and Yamada 1974; Estoque and Bhumralkar 1970; Lee and Olfe 1974, Sheih and Moroz 1975; Torrance and Shum 1976) use

$$l = \frac{\kappa z}{1 + \dfrac{\kappa z}{\lambda}} \tag{32}$$

Louis (1979) used the constant value of λ = 100 m, but Thompson and Williams (1997) found that λ = 150 m for K_m and λ = 350 m for K_h were more typical for frontogenesis. Note that in equation (32) l is proportional to height near the surface, but approaches a reference value of λ at higher elevations. This is physically reasonable since near the surface, the size of eddies is constrained by distance to the surface, and l should not

increase without bounds with elevation. Over the range of slightly negative and positive RI, the resulting distribution is approximated by

$$K_m = K_h = 0 \qquad\qquad , \text{Ri} > \text{Ri}_c$$

$$K_m = K_h = 1.1\left(\frac{Ri_c - Ri}{Ri_c}\right)l^2\left|\frac{\partial V}{\partial z}\right| \quad , \text{Ri} \le \text{Ri}_c \qquad\qquad \textbf{(33)}$$

where the critical Richardson number is $\text{Ri}_c = 0.25$ (Blackadar 1979). Following Keyser and Anthes (1982), the coefficients are broken into a small, constant diffusive part K_{z0} and a variable part modeled after equation 33

$$K_m = K_h = K_{z0} \qquad\qquad , \text{Ri} > \text{Ri}_c$$

$$K_m = K_h = K_{z0} + \kappa^2 l^2\left|\frac{\partial V}{\partial z}\right|\left(\frac{Ri_c - Ri}{Ri_c}\right) \quad , \text{Ri} \le \text{Ri}_c \qquad\qquad \textbf{(34)}$$

where l is calculated from equation (32) with $\lambda = 150$ m for K_m and $\lambda = 350$ m for K_h. Finite differencing tends to give greater values of Ri than the mean Ri within the layer (Blackadar 1979), so $\text{RI}_c = 1.0$ vice the theoretical value of 0.25 to account for the finite grid resolution (following Keyser and Anthes 1982).

D.   FOURTH ORDER DIFFUSION

In the control run, the model's fourth order diffusion constants are given a value of 0.5×10^{-5} at the surface that increases linearly in the vertical to 0.5×10^{-4}. This linear increase maximizes the damping of small-scale numerical noise through the domain without giving excessive surface diffusion and it helps to control the reflection of energy from the rigid upper boundary. This distribution is not as heavy handed as a traditional sponge.

In the simulations including the planetary boundary layer, the fourth order diffusion coefficients are defined following Keyser and Anthes (1982) as

$$K = (\Delta x)^2 \left\{ 10 X 10^4 + \frac{1}{2}\kappa^2(\Delta x)^2 \left[\left(\frac{\partial u}{\partial z}\right)^2 + \left(\frac{\partial v}{\partial z}\right)^2\right]^{\frac{1}{2}} \right\} \qquad\qquad \textbf{(35)}$$

Horizontal and vertical diffusion coefficients for u, v, and θ are given equal values within the model.

THIS PAGE INTENTIONALLY LEFT BLANK

III.   FRONTOGENETIC FORCING

The mechanisms that concentrate wind and temperature into a tight zone in a frontal region can be explained by examining the individual terms of the frontogenetical function, written as

$$\frac{\partial}{\partial x}\frac{\partial \theta}{\partial t} = F_{adv} + F_{con} + F_{tilt} + F_{sh} + F_{PBL} \tag{37}$$

where

$$F_{adv} = -u\frac{\partial}{\partial x}\left(\frac{\partial \theta}{\partial x}\right) - w\frac{\partial}{\partial z}\left(\frac{\partial \theta}{\partial x}\right) \tag{38}$$

$$F_{con} = -\frac{\partial u}{\partial x}\frac{\partial \theta}{\partial x} \tag{39}$$

$$F_{tilt} = -\frac{\partial w}{\partial x}\frac{\partial \theta}{\partial z} \tag{40}$$

$$F_{sh} = -\frac{\partial v}{\partial x}\frac{\partial \theta}{\partial y} \tag{41}$$

$$F_{PBL} = \frac{\partial}{\partial x}\frac{\partial}{\partial z}\left(K\frac{\partial \theta}{\partial x}\right) + \frac{\partial}{\partial x}\frac{\partial}{\partial z}\left(K_h\frac{\partial \theta}{\partial x}\right) = \frac{\partial}{\partial x}(Q) \tag{42}$$

F_{adv} (38) represents the advection term. The convergence term (39) quantifies the effect of u on isentropes in reducing or concentrating the temperature gradient. The tilting term (40) quantifies the effect of a gradient of vertical motion tilting the isentropes into a vertical plane.   Shear deformation (41) quantifies the effect of the v wind on the north-south horizontal gradient in the isentropes. F_{PBL} (42) represents forcing due to planetary boundary layer diffusion, 4th order diffusion, surface momentum flux and surface heat flux.

THIS PAGE INTENTIONALLY LEFT BLANK

IV. NUMERICAL RESULTS

The results from the numerical simulations are discussed in the following sections. The emphasis of this study is on the comparison of the inviscid case results to those of the planetary boundary layer simulations which were run with the same initial conditions. Table 2, summarizes the simulations conducted with 10 km horizontal resolution and $\Delta t = 30$ s. Simulations A and C are run at 5 km horizontal resolution with a $\Delta t = 10$ s.

Simulation	A	B	C	C1	C2
Momentum flux	No	Yes	Yes	Yes	Yes
z_0	-	$z_0 = 0.4$ m	Calculated	Calculated	Calculated
Heat Flux	No	No	Yes	Yes	Yes
SST	-	-	$\theta_1 \sim 282$ K	287 K	$\theta_1 \sim 282$ K
z_{0h}	-	-	Calculated	Calculated	Calculated
4th order diffusion	0.5×10^{-5} increasing linearly vertical to 0.5×10^{-4}	Eq (36)	Eq (36)	Eq (36)	Eq (36)
PBL diffusion	No	Eq (35)	Eq (35)	Eq (35)	$K_m = K_h = 1.0$

Table 2.   Numerical Simulations

A.   ADIABATIC AND INVISCID SIMULATION (A)

The model is run first with the surface flux and boundary layer parameterizations excluded to serve as a control case. The case is nearly inviscid in the sense that fourth order horizontal diffusion is always present. The initial u and θ fields are shown in

Figure 1 as functions of x and z. The cross frontal velocity field in Figure 1a (and all subsequent figures) includes the mean background flow.

Due to the baroclinically unstable initial state, rapid frontogenesis may be anticipated. Figure 2 contains the frontal solutions after 108 hours of integration. Only the lower portion of the atmosphere is shown to highlight the near-surface effects and only a 1500 km horizontal extent surrounding the front is shown to closely examine the area around the front. The front has intensified and all fields have been advected downstream with the background current. The vertical motion field, Figure 2c, shows ascending motion all ahead of the front with weak descending motion in the cold air behind the front giving a thermally direct circulation about the front. Also the v field shows large cyclonic vorticity just east of the maximum temperature gradient (Figure 2b).

Figure 2.   Inviscid frontal solutions at t = 108 h: (a) cross-front flow, m s^{-1}; (b) along-front flow, m s^{-1}; (c) vertical velocity, m s^{-1}; (d) potential temperature, deg K.

Rapid frontogenesis continues since the north-south temperature gradient does not change. Figure 3 contains the frontal solutions after 120 hours of integration. The front has continued to intensify. The v field indicates increased horizontal shear and there is an increased horizontal temperature gradient (Figure 3b-c). The front is strongest at the surface as indicated by the increased horizontal temperature gradient in that region. The southerly wind ahead of the front is bringing in warm air while the northerly wind behind the front is bringing down cold air from the north (Figure 3b,d).
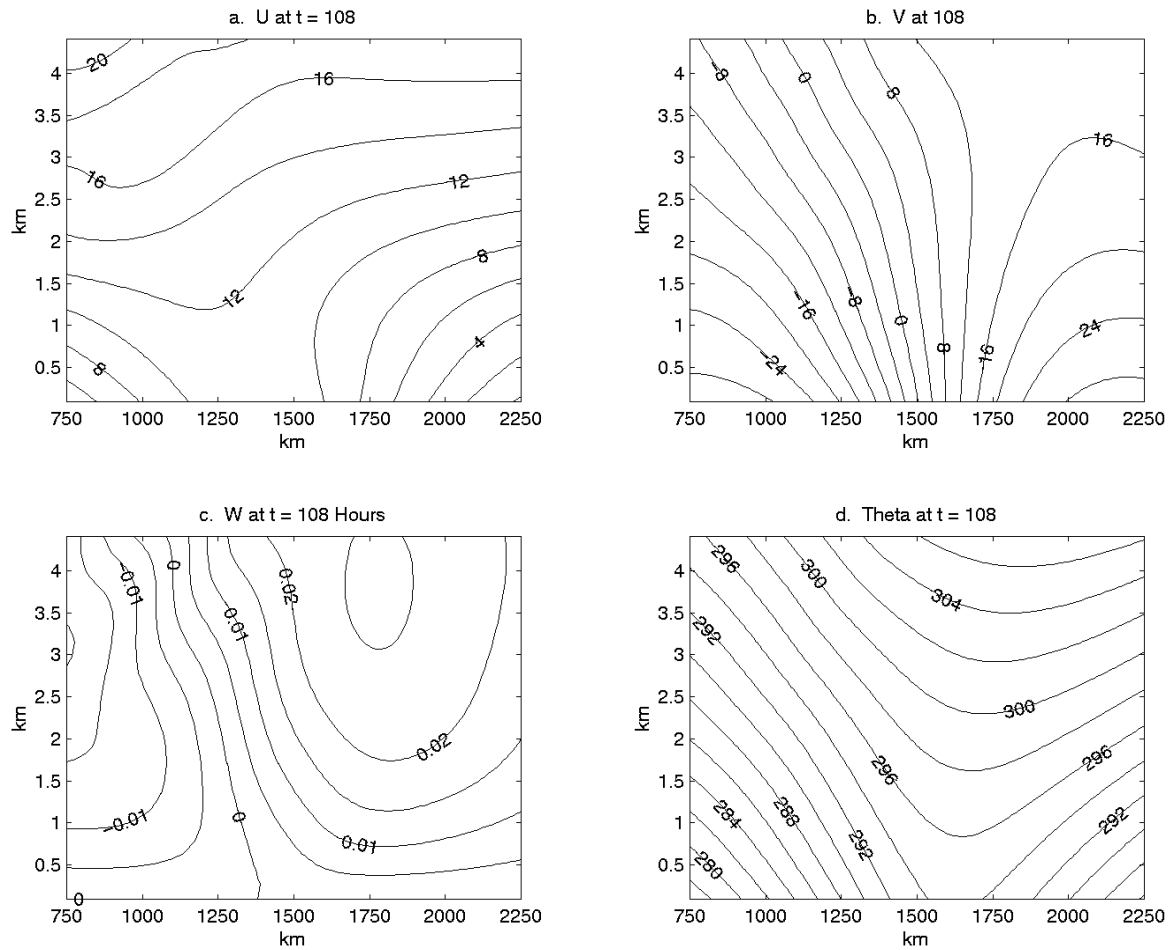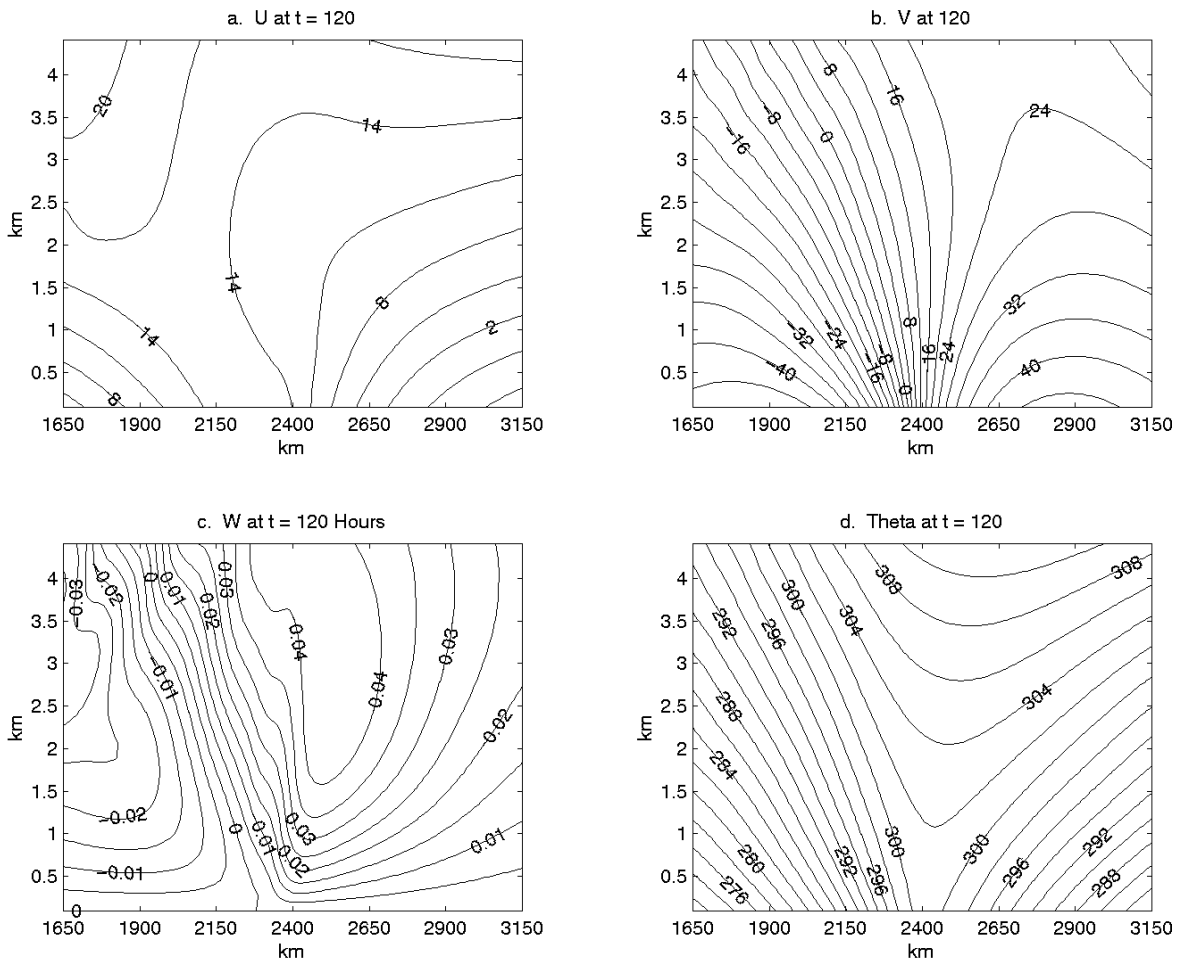

Figure 3. Inviscid frontal solutions at t = 120 h: (a) cross-front flow, m s^{-1}; (b) along-front flow, m s^{-1}; (c) vertical velocity, m s^{-1}; (d) potential temperature, deg K.

Figure 4 is a comparison of the frontogenetic forcing terms F_{sh}, F_{tilt} and F_{con} at t = 108 h and t = 120 h with different scales. Values of the frontogenetic equation indicate

that, while the wave is small amplitude, the main forcing is due to F_{sh}. Opposing this frontogenesis is the F_{tilt} term. Because this term goes to zero at the surface the front is strongest at the surface and weaker above. Convergence in the u field has continued to become stronger. As the wave grows in amplitude F_{con} will contribute more to frontogenesis than F_{sh}. Also note that the maximum values of F_{sh} and F_{con} are to the east of the maximum temperature gradient region. This causes the front to move to the east relative to the mean flow, which allows it to keep its upwind vertical tilt.
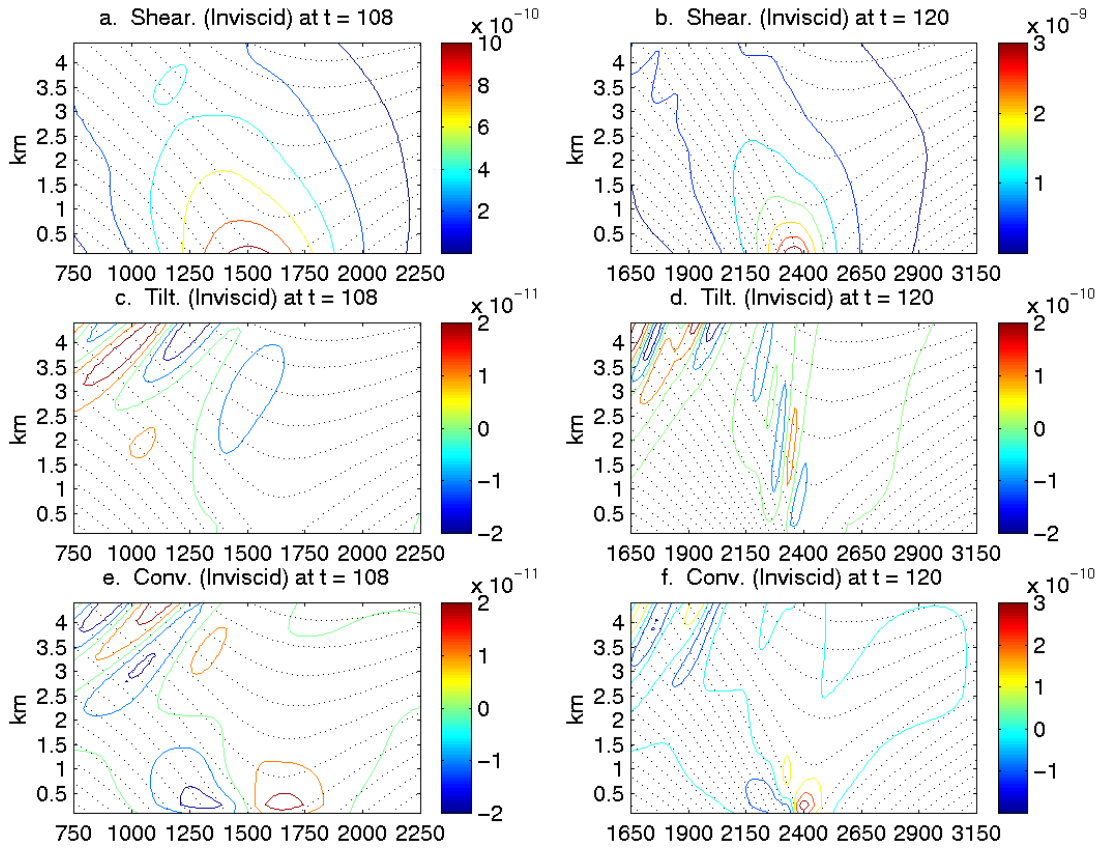
Figure 4. Frontogenetic forcing terms for inviscid simulation: (a) F_{sh} at t = 108 h; (b) F_{sh} at t = 120 h; (c) F_{tilt} at t = 108; (d) F_{tilt} at t = 120 h; (e) F_{con} at t = 108 h; (f) F_{con} at t = 120 h; the potential temperature lines (dashed) are included for reference.

To quantify the scale of the frontal zone, the parameter D is defined as

$$D = \frac{|\Delta\theta|}{\left|\dfrac{\partial\theta}{\partial x}\right|_{max}} \tag{36}$$

where $\Delta\theta$ is the maximum horizontal temperature variation at that level. Because D is a measure of the temperature gradient and no friction is considered, it is expected to oscillate when no frontogenesis occurs and to collapse when a front forms. The frontal scale for both the frictionless and PBL land cases is presented in Figures 5 and 6. Figure 5 gives a comparison at 90 m and Figure 6 gives a comparison at 1.35 km. At t = 168 h, the D = 34.7 km at 90 m and D = 55.5 at 1.35 km. This is due to the fact that the tilting term is frontolytic, but goes to zero at the surface. Since the frontolytic effect decreases towards the lower boundary the frontal scale is smaller at 90 m.
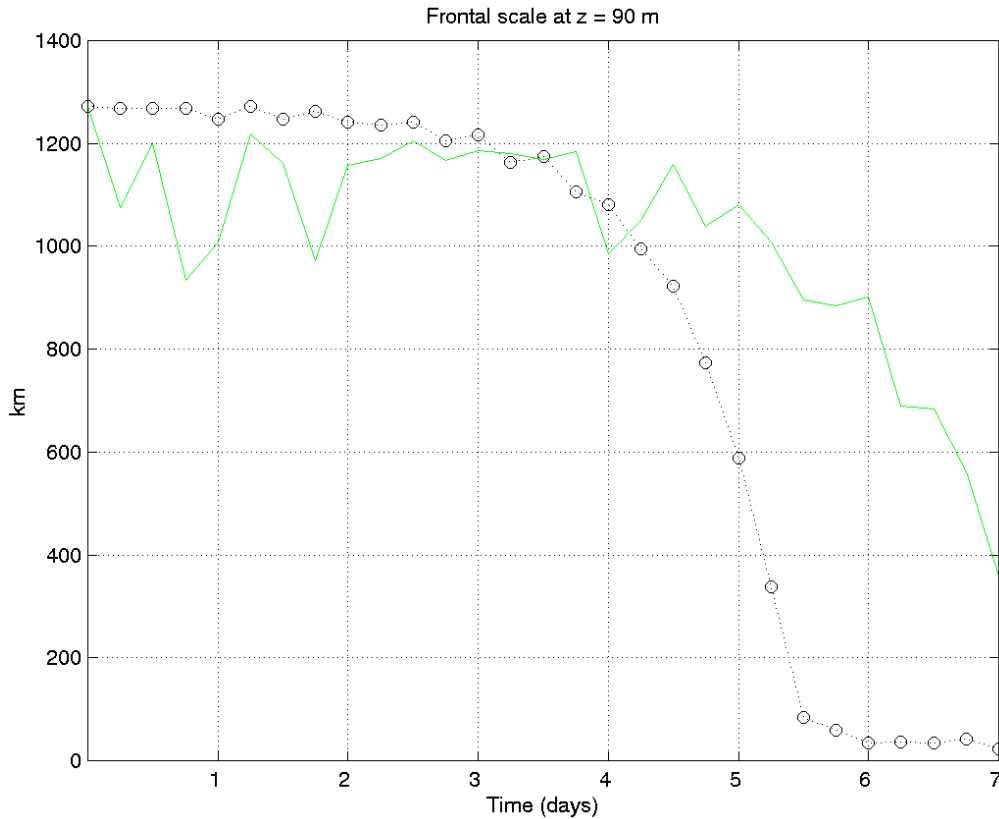
Figure 5.   Frontal scale parameter at 90 m: dotted black line with o: case A (inviscid); solid green line: case B (PBL over land).

21
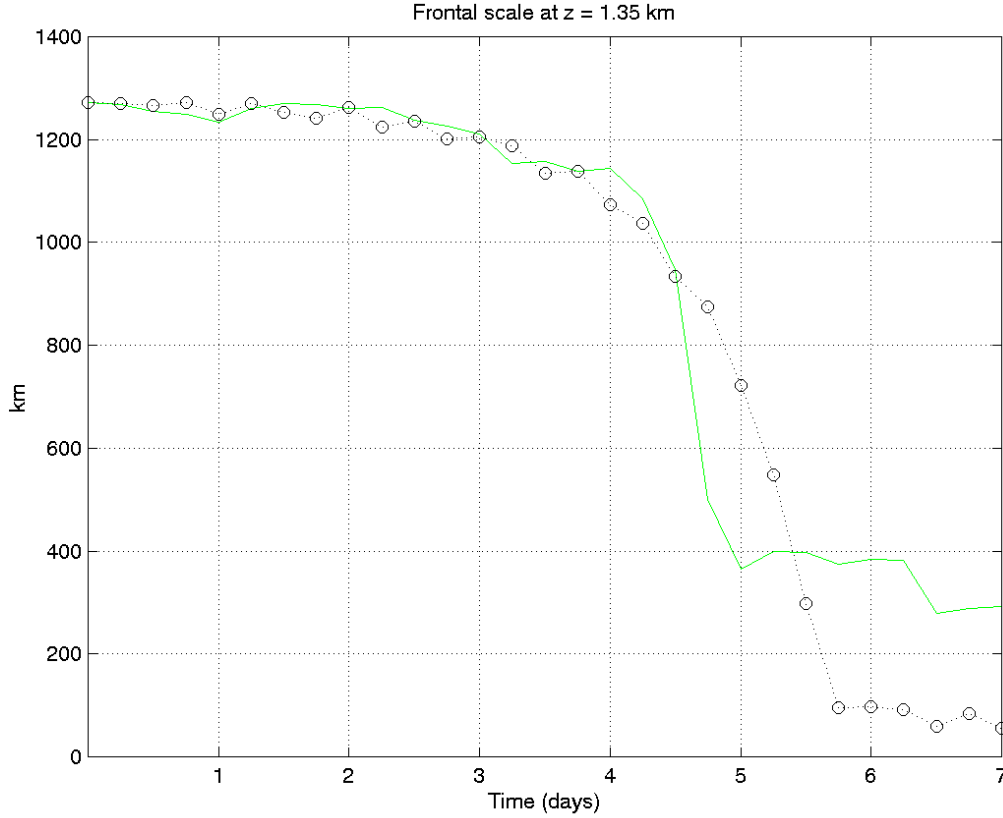
Figure 6.   Frontal scale parameter at 1.35 km: dotted black line with o: case A (inviscid); solid green line: case B (PBL over land).

Figure 7 shows a time series of the maximum along-front flow in the lowest 16 levels of the model (2.79 km) for the present case (A), the K-theory boundary layer land case (B) discussed in section 3.2 below, and the K-theory boundary layer ocean case (C) described in section 3.3 below. Note the rapid intensification beginning near 72 hours. Figure 4 contains the frontal solutions after 120 hours of integration when the front is extremely strong. The vertical circulation has increased slightly. The ascent ahead of the front at t = 108 h is only 0.027 m s^{-1} (Figure 2c), but by t = 120 it has increased to 0.044 m s^{-1} (Figure 3c). At this point the along-front velocity, as shown in Figure 7, is becoming unrealistic. Because the north-south temperature gradient, $\partial\theta/\partial y$, does not change, this front will continue to grow.

22
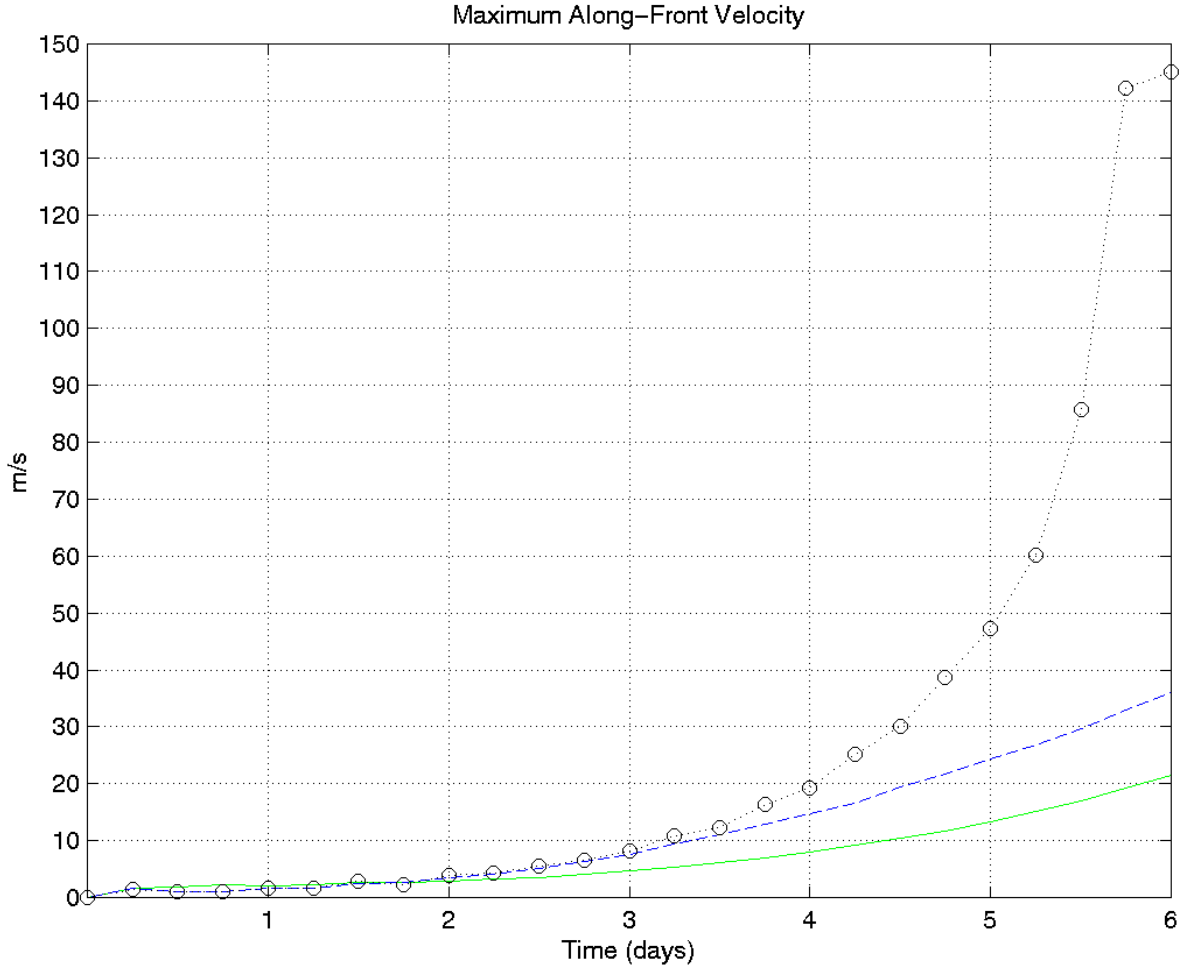
Figure 7.   Maximum along-front velocity from the surface to 2.79 km; dotted black line with o: case A (inviscid); dashed blue line: case C (PBL over ocean); solid green line: case B (PBL over land).

These results clearly show that in the absence of boundary layer processes, a growing baroclinic wave will generate a strong front at the surface.   However this simulation is unrealistic because along frontal wind velocities exceed 60 m s^{-1} by t = 126 h (Figure 7). In addition, the circulation and vertical motion about the front is too weak. During the Storm Transfer and Response Experiment (STREX) in November 1980 vertical motion fields for a cold front were observed by aircraft to be 6 m s^{-1} in the updraft and 2 m s^{-1} in the downdraft (Bond and Fleagle 1985).

To determine whether a smaller scale front could be achieved, simulation A was run at Δx = 5 km. Figure 8 shows a time series of frontal scale calculated with (36) for

both horizontal resolutions. After t = 126 h, frontal scale for the Δx = 5 km solution begins to deviate from the Δx = 10 km solution and become smaller. By t = 180 h, D = 11.1 km for Δx = 5 km and at t = 168 h, D = 23.1 km for Δx = 10 km. Clearly smaller scale fronts can be achieved using a higher resolution model. Similar numerical results were obtained by Williams (1967).
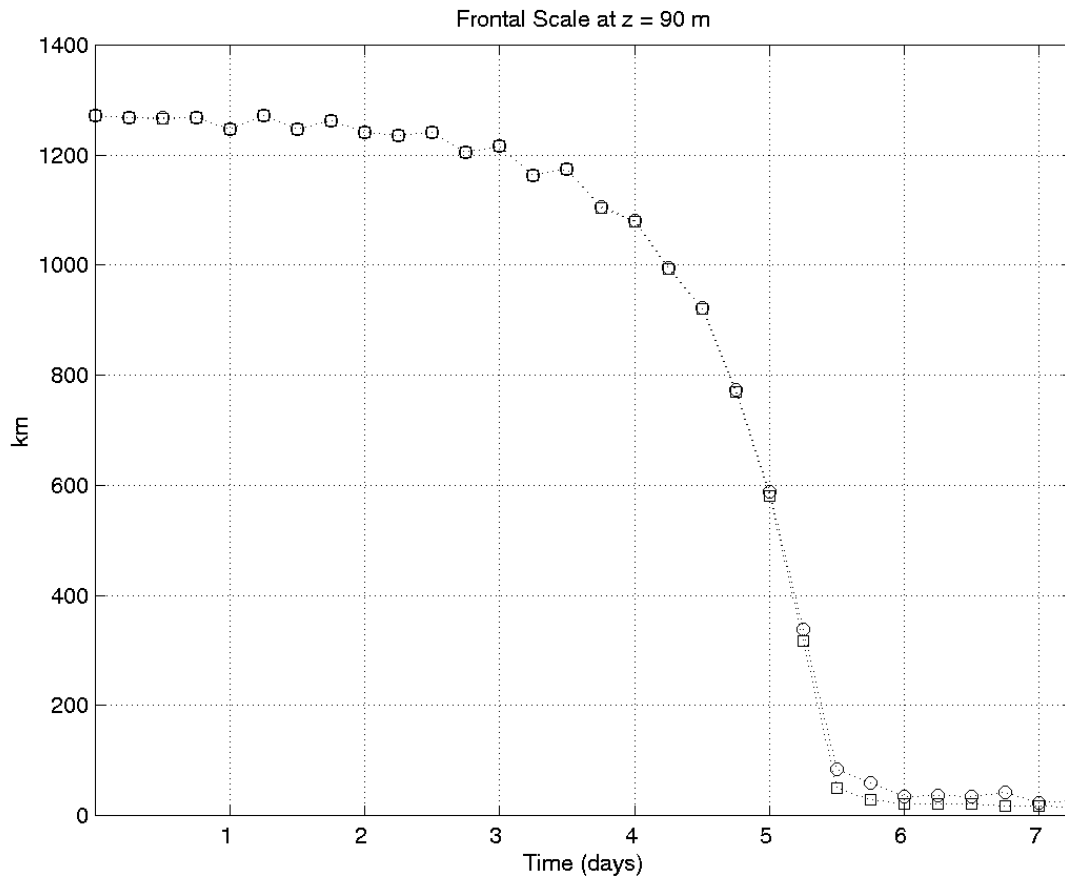
Figure 8.   Frontal scale at z = 90 m: black dotted with o: Δx = 10 km; black dotted with □: Δx = 5 km.

B.   LAND SIMULATION

For this experiment, the initial conditions are identical to those in the adiabatic and inviscid case. A typical value for woodland area of 0.4 m (Garrett 1980; Fichtl and McVehil 1970) is assigned to z_0. Since sensible heat flux is small over land except for during daylight hours, sensible heat flux is neglected at the lower boundary in this case to idealize land without a diurnal cycle.

24

Figure 9 compares the potential temperature fields at t = 6 h for cases A and B. By t = 6 h, a well-mixed layer is already developed in the PBL land case (Figure 9b). The potential temperature gradient associated with the front is much different in this simulation than in the inviscid case. The well-mixed layer continues to develop and deepen in the PBL land case through t = 126 h (not shown).
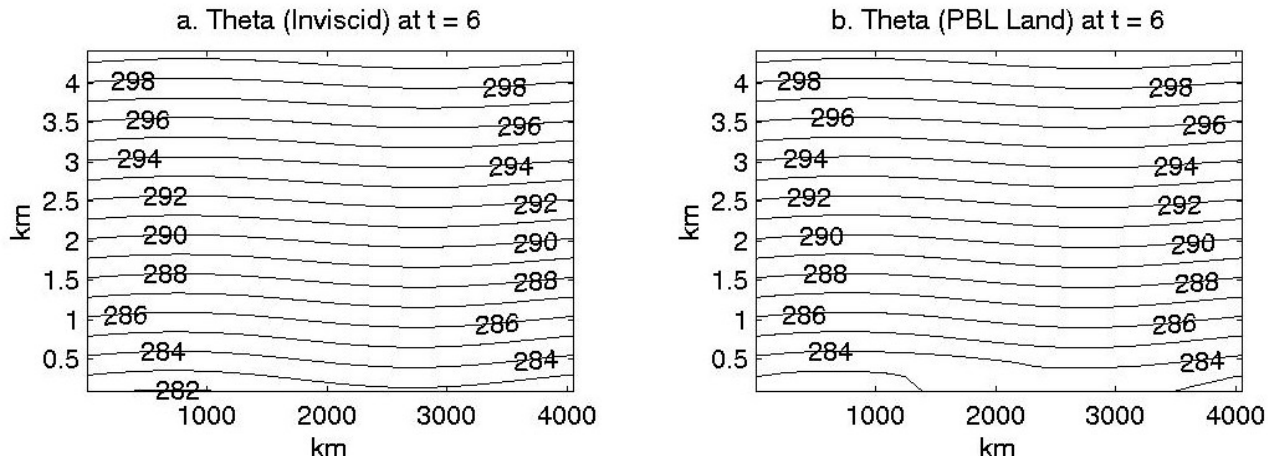
Figure 9. Potential temperature fields at t = 6 h: (a) inviscid case; (b) PBL land case.

Figure 10 presents frontal solutions for the PBL land case at t = 108 h. The frontal zones depicted in the potential temperature fields at t = 108 h exhibit no tilt in the vertical from the surface to approximately 1 km (Figure 10d). The well-mixed areas on both sides of the front prevent tilt. This is in contrast to the inviscid case in which the frontal zone has pronounced tilt (Figure 2d). The location of the maximum along-front wind speed is no longer at the surface, but at approximately 1 km at t = 108 h (Figure 10b) with lower wind speeds near the surface. In addition the overall maximum wind speed is lower (Figure 7). The lower wind speed near the surface can be attributed to surface drag. This case is similar to the cases treated by Keyser and Anthes (1982) and Peng *et al*. (2001).

The effect of the addition of surface momentum flux is clear from Figures 5 through 10. Surface momentum flux produces a well-mixed surface layer, reduces the along-front velocity and reduces the growth of the baroclinic wave since the frontal scale is larger in the PBL land case. In addition at the surface, it takes longer for the

frontogenesis to begin and for the PBL front to develop. The PBL frontal scale is smaller above the surface as seen by the lower value of D.
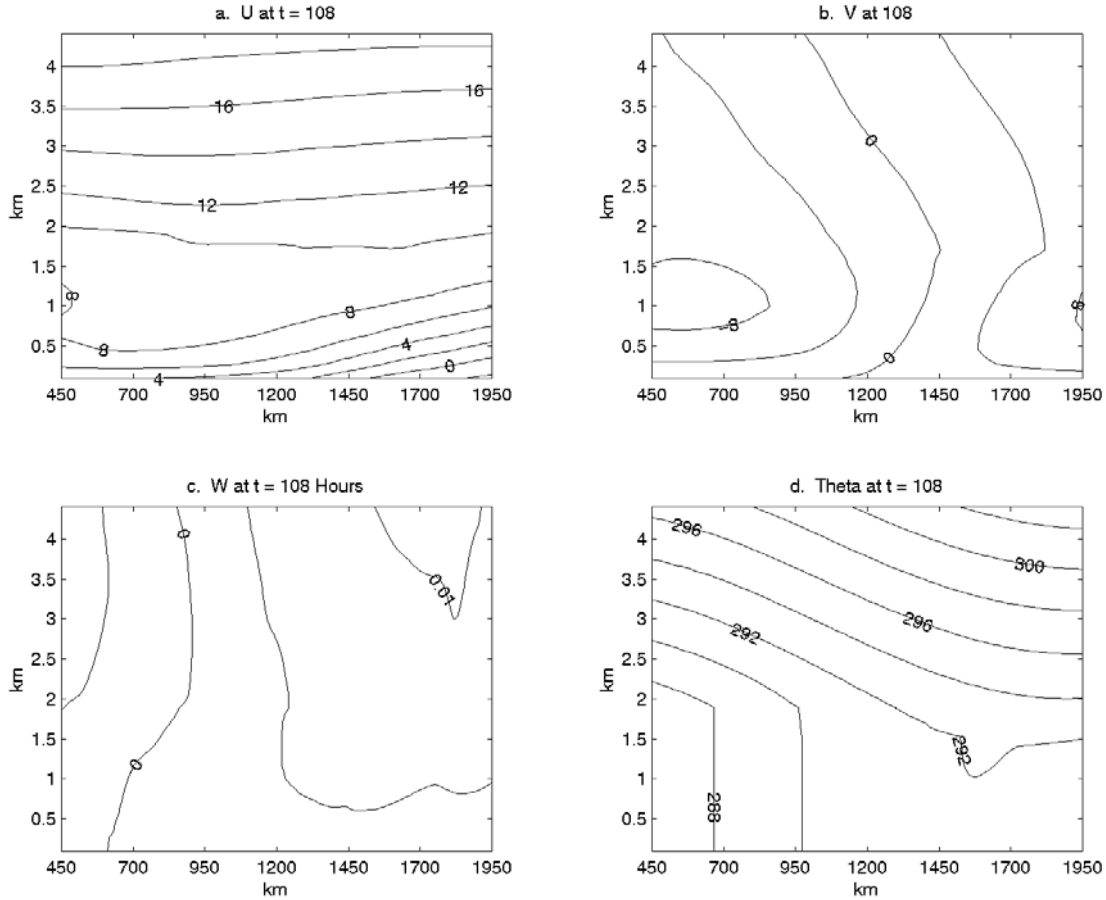
Figure 10.   PBL frontal solutions at t = 108 h: (a) cross-front flow, m s^{-1}; (b) along-front flow, m s^{-1}; (c) vertical velocity, m s^{-1}; (d) potential temperature, deg K.

The baroclinic wave amplitude is smaller in this case and the potential temperature gradients associated with the front are different from the inviscid simulation. There are several reasons for this. Looking at the frontogenetic terms, F_{PBL} becomes more important in this simulation since surface momentum flux and PBL diffusion have been added. The effect of F_{PBL} is frontolytic. Figure 11 displays F_{sh} for the inviscid and PBL land simulations at t = 72 h with different scales. This time period was chosen because in the inviscid simulation after t = 72 h the front intensifies rapidly. F_{sh} has the

same order of magnitude in each simulation, but for the PBL case the maximum frontogenetic effect is not at the surface and is about one half the magnitude of the inviscid case. The overall frontogenetic effect is reduced further in the PBL case because PBL diffusion is frontolytic. Figures 5 and 6 indicate that the frontal scale for the PBL case was smaller at 1.35 km than at 90 m. This is due to the frontogenetic effect of F_{sh} going to zero at the surface since it is proportional to v.
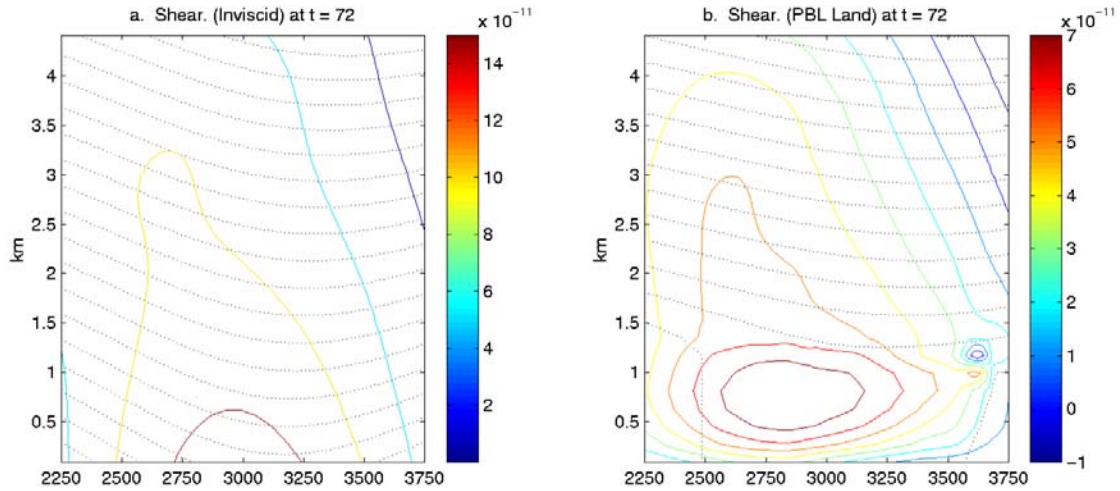
Figure 11. F_{sh} at t = 72 h: (a) inviscid simulation; (b) PBL land simulation.

C.   OCEAN SIMULATIONS (C, C1, C2)

Three ocean simulations are conducted. In cases C and C2, the sea surface temperature is set equal to the air temperature at the lowest model level at the initial time. It is fixed at this value for the duration of the model run. For case C1, the sea surface temperature is set to 287 K which is approximately 5 degrees warmer than for the other simulations. In case C2, virtually all PBL diffusion is removed by setting $K_m = K_h = 1.0$ at all grid points except at the lowest level.

Figure 12 shows a time series of the maximum along-front wind for all ocean simulations and the inviscid simulation. As expected in the case with the warmer sea surface temperature, the frontal scale is not as small as in the simulation run with the colder water due to decreased mixing. Figure 13 illustrates a time series of maximum K_m for simulations B, C and C1. Until t = 80 h, K_m values are largest for the land simulation indicating the strongest mixing. K_m values are larger for the warm water simulation than

the cooler water simulation up until t = 80 h. Case C2 with small planetary boundary layer diffusion more closely approaches the inviscid case, but because of the addition of the surface momentum and heat fluxes it is not as strong.
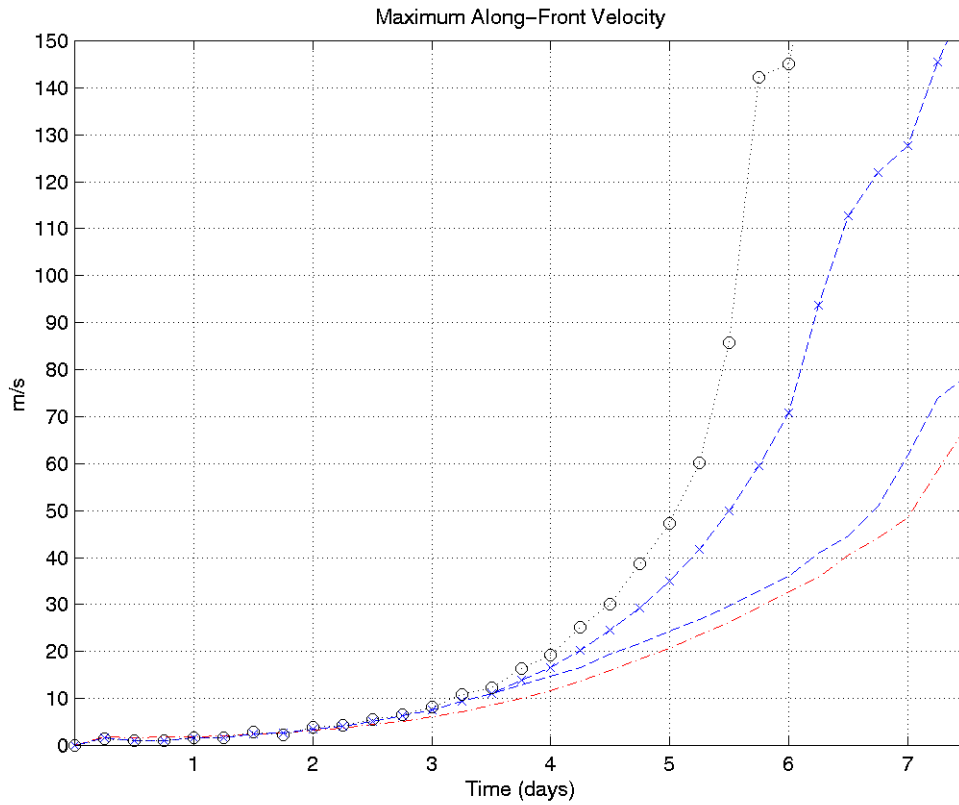
Figure 12.   Maximum along-front velocity from the surface to 2.79 km: dotted black with o: inviscid simulation (case A); dashed blue with x: ocean simulation with small PBL diffusion (case C2); dashed blue: ocean simulation with 282K SST (case C); dash-dot red: ocean simulation with 287K SST (case C1).
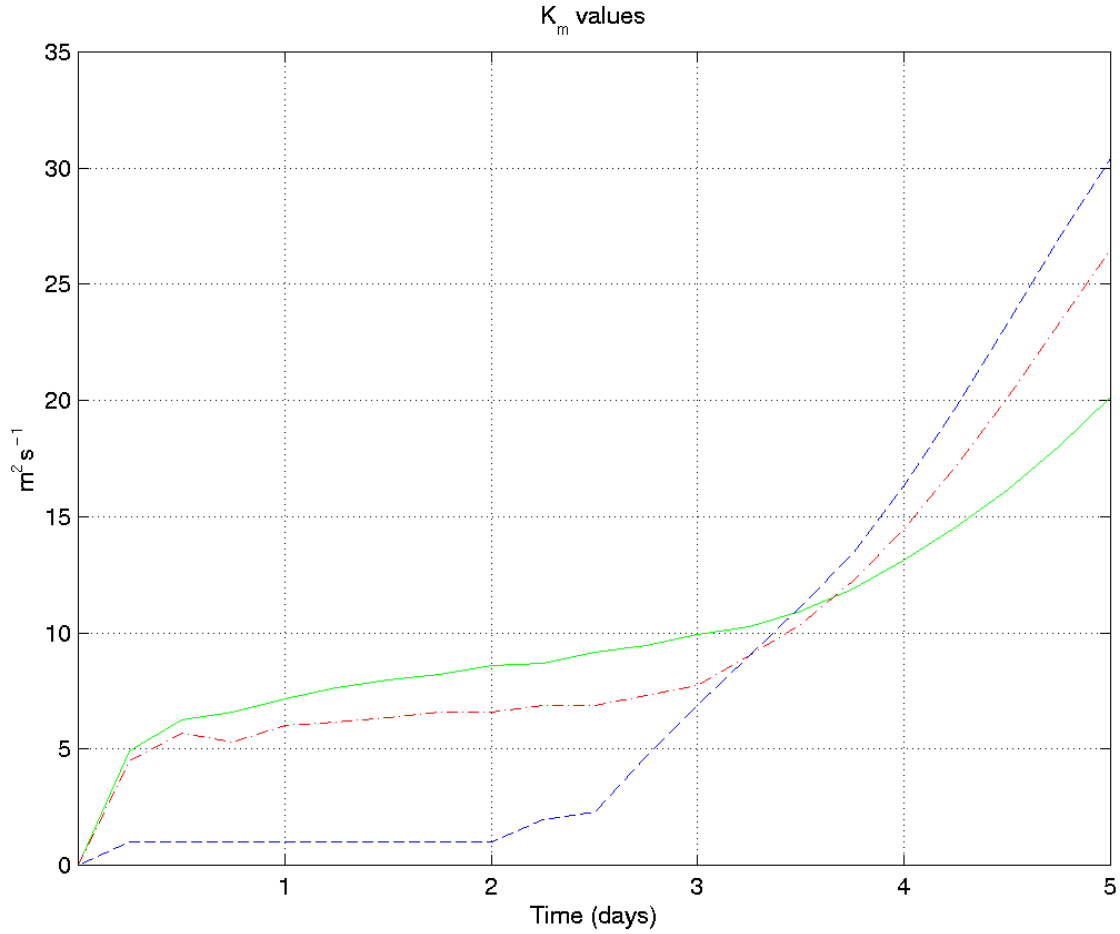
Figure 13. K_m values: green solid: PBL land simulation (case B); dashed blue: ocean simulation with 282K SST (case C); dash-dot red: ocean simulation with 287K SST (case C1).

Figure 14 shows the time evolution for frontal scale as defined by (36) for the ocean simulations and the inviscid simulation. Although the along-front velocity in all ocean simulations is less than in the inviscid simulation, from t = 72 h until t = 114 h (Figure 14) the frontal scale is smaller in the ocean simulations.
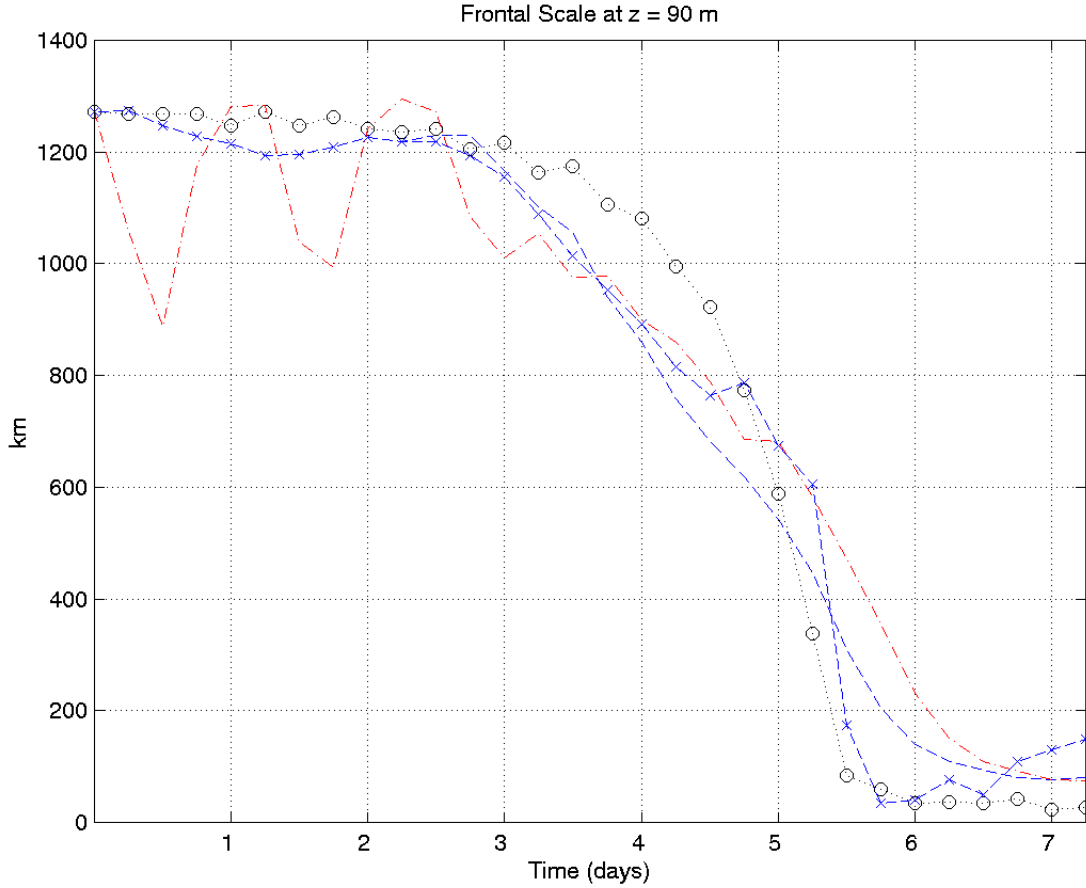
Figure 14.   Frontal scale at z = 0.9 km: dotted black with o: inviscid simulation (case A);
dashed blue with x: ocean simulation with no PBL diffusion (case C2); dashed blue:
ocean simulation with 282K SST (case C); dash-dot red: ocean simulation with 287K
SST (case C1).

In the ocean simulations it takes longer for the well-mixed layer to develop than
in the PBL land simulation. At t = 12 h, cases C and C2 are just starting to form a well-
mixed layer while case C1 already has (not shown). The larger upward heat flux
associated with the warmer seawater in case C1 is causing more turbulence and stronger
mixing in the surface layer than in the cooler SST cases. Remember that in the PBL land
simulation, a well-mixed layer was formed by t = 6 h (Figure 9), but as expected in the
ocean simulations it takes longer. The delay in the formation of this well-mixed layer can
be attributed to the dependence of surface heat and momentum fluxes on the surface
roughness lengths and in these cases z_o (.001 - .002 m) is significantly smaller than the
0.4 m used in the PBL land simulation.

1.   Effect of Planetary Boundary Layer Diffusion and Surface Fluxes

By comparing potential temperature fields for cases C and C2, the timing for when boundary layer diffusion (35) begins to have an influence can be determined. Potential temperature fields for these cases are identical up until t = 66 h (not shown) and frontal scale measured by D is equal through t = 54 h (Figure 14). By examining eddy viscosities values, K_m and K_h, as defined by (35), it becomes apparent that boundary layer diffusion only affects case C after t = 54 h when K_m and K_h exceed 1. The greater values of K_m and K_h after t = 54 h are consistent with larger values of u_*. Figure 15 shows the frontal solutions at t = 108 h for cases C and C2. Adding the K-theory boundary layer parameterization results in a more realistic θ pattern. The potential temperature gradient across the front is larger in C compared to C2 (Figure 15g-h). This potential temperature gradient remains well defined in case C despite boundary layer friction. These parameterizations also result in more realistic along-front velocity fields. While C2 is more realistic than the inviscid simulation, it still continues to grow and produces unrealistic along-front velocities that exceed 60 m s^{-1} after 5.5 days. The addition of boundary layer diffusion in case C produces a reasonable along-front wind velocity of 36 m s^{-1} at day 6.

Figure 13 indicated that higher heat flux in case C1 produced larger K_m values up until t = 80 h. After t = 80 h, case C K_m values are larger than case C1

Comparison of Figure 15 to the corresponding frontal solution for the inviscid simulation (Figure 2) clearly shows the influence of the boundary layer diffusion, surface momentum flux and heat flux. There is clear evidence of the frontal structure in the temperature fields for the ocean simulations. The strongly stratified cold air behind the front in the inviscid simulation is replaced in these simulations by a well-mixed layer approximately 1 km deep for case C and 0.5 km deep for case C2. Strong surface fluxes in the unstable air behind the front in case C promote entrainment and a greater deepening of the boundary layer than case C2. The frontal zones depicted in the potential temperature fields (Figure 15g-h) exhibit no tilt in the vertical over this well-mixed layer. This is in contrast to the inviscid simulation, but it agrees with strong fronts observed

31

over the ocean (Bond and Fleagle 1985; Fleagle *et al.* 1988; Chien *et al.* 2001). The lack of tilt is due to well-mixed boundary layers on both sides of the front.
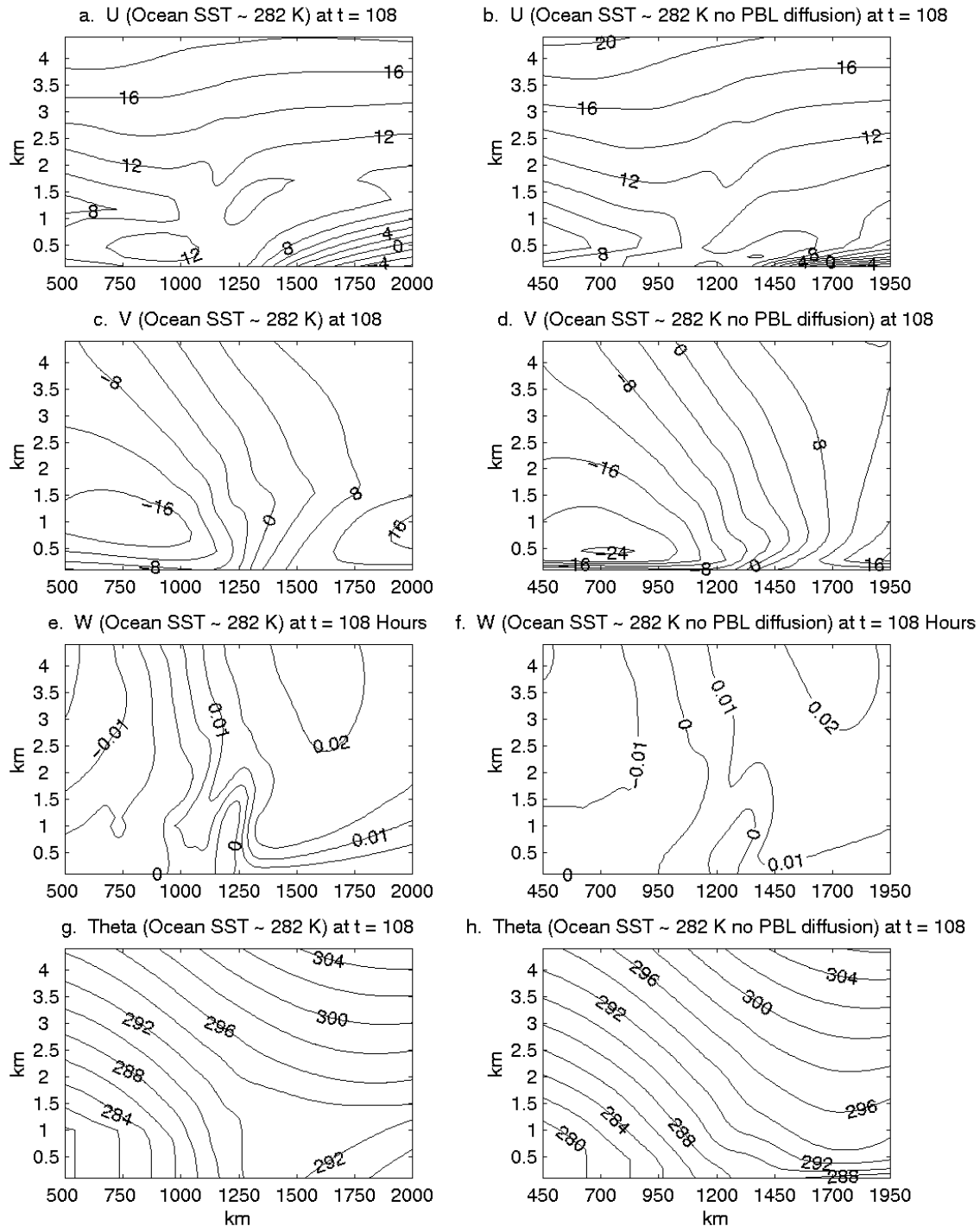

Figure 15. Frontal solutions for cases C and C2 for t = 108 h: (a) U (m s^{-1}) for ocean simulation SST ~ 282 K (case C); (b) U (m s^{-1}) for ocean simulation SST ~ 282 K no PBL diffusion (case C2); (c) V (m s^{-1}) for case C; (d) V (m s^{-1}) for case C2; (e) W (m s^{-1}) for case C; (f) W (m s^{-1}) for case C2; (g) Theta (K) for case C; (h) Theta (K) for case C2.

32

2.   Frontal Scale

Figure 16 shows a time series of frontal scale calculated with (36) for both horizontal resolutions for case C. After t = 126 h, frontal scale for the Δx = 5 km begins to deviate from the Δx = 10 km and become smaller. By t = 168 h, D = 54.5 km for Δx = 5 km and at t = 168 h, D = 76.2 km for Δx = 10 km. Clearly smaller scale fronts can be achieved using a higher resolution model. During the PBL land simulation with z_o= 0.4 m, the smallest D reached was D = 136.6 km at t = 186 h. The simulations conducted produced smaller scale fronts over the ocean than over land.
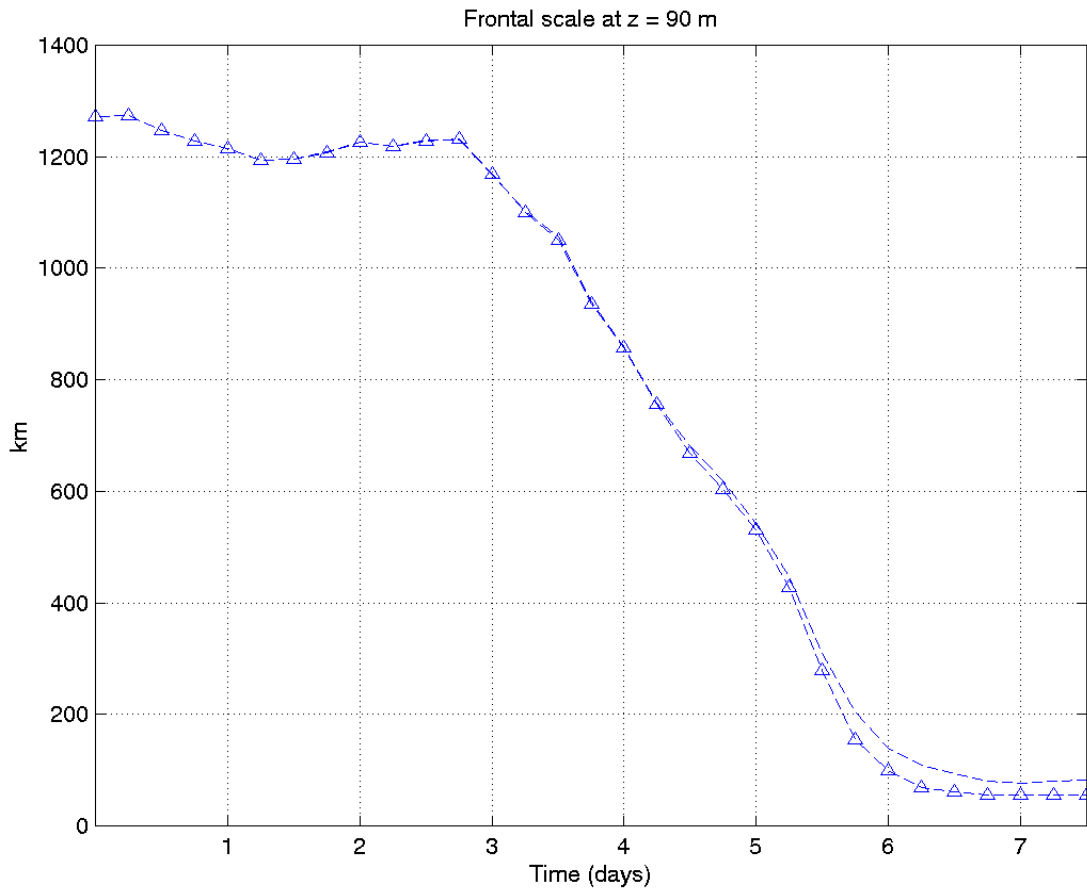
Figure 16.   Frontal scale at z = 90 m: blue dashed: Δx = 10 km; blue dashed with Δ: Δx = 5 km.

3.   Frontogenetic Forcing in the Ocean Simulations

As in the inviscid simulation, values of the frontogenetic equation indicate that the main forcing in the ocean simulations while the wave is small amplitude is due to F_{sh}. Opposing this frontogenesis is the F_{tilt} term. Convergence in the u field becomes stronger

33

as the wave amplifies. As the wave grows in amplitude, F_{con} will contribute more to frontogenesis than F_{sh}. Figure 17 shows F_{con} normalized by the absolute value of F_{sh} for the inviscid simulation and the ocean simulation, C. When F_{con} is normalized by the absolute value of F_{sh} exceeds 1, F_{con} is contributing more to frontogenesis than F_{sh}. F_{con} contributes to frontogenesis more than F_{sh} only after 5.5 days for both cases. For the inviscid simulation, F_{con} grows significantly faster than in the ocean simulation in which frictional effects decrease the wind speed at low levels and increase low-level cross-isobaric flow. The frontogenetic effect of F_{con} in the inviscid simulation exceeds F_{sh} approximately 6 hours prior than in the ocean simulation.

Figure 17. F_{con} normalized by the absolute value of F_{sh}: solid with *: inviscid simulation (Case A); dashed black: ocean simulation with 282K SST (Case C).

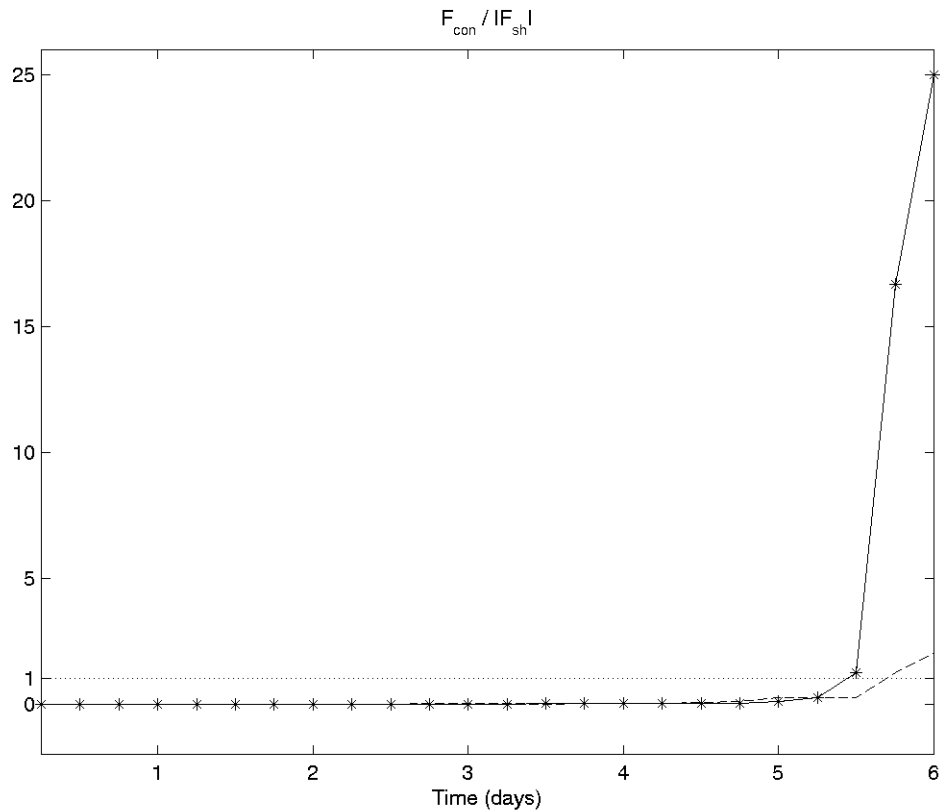   Other terms in the frontogenetic equation become important in the ocean simulations since surface momentum flux, surface heat flux and PBL diffusion have been added. Because all simulations are thermally direct circulations, the tilting term is

predominantly frontolytic east of the front because of the distribution of vertical motion. As the vertical motion fields become more compact and the maximum in vertical motion moves closer to the lower boundary the F_{tilt} gets a dipole structure as seen in Figure 18. Larger gradients in vertical motion produce larger magnitude in the tilting term. The largest gradient in vertical motion is within the frontal zone where the vertical motion changes sign. In Figure 18, this area causes a reversal in direction of the gradient in vertical motion and results in a frontogenetic contribution from the tilting term. In the ocean simulations, after t = 96 h an area of weak sinking develops east of the frontal zone. During the ocean simulations, the tilting term increases 3 orders of magnitude in the frontal region by t = 144 h. While the tilting term does this in the inviscid simulation, by t = 144 h F_{tilt} is still 3 orders of magnitude smaller than the shear term. For the ocean simulation by t = 144 h, F_{tilt} is only one order of magnitude smaller than F_{sh}.
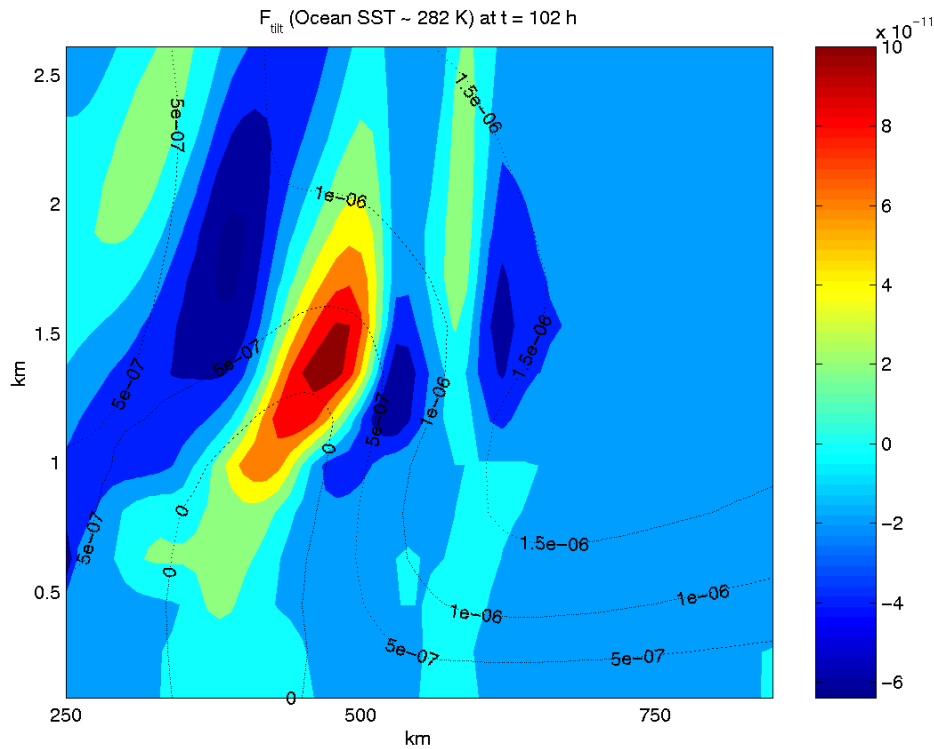

Figure 18. F_{tilt} at t = 102 h for case C: dotted black: W (m s^{-1}).

4.   Effect of Sea Surface Temperature

In an attempt to determine frontal structures as a function of the air-sea temperature, the simulation C1 was conducted with an initial sea surface temperature

(SST) of 287 K which is approximately 5 K higher than the SST in simulation C. Because the air in this simulation is colder than the water, a deeper mixed layer is expected behind the cold front then was seen in simulation C. Due to the increased turbulent mixing in case C1 less frontogenesis is expected than for case C.

Figure 19 shows the frontal solutions at t = 108 h for cases C and C1. As expected the warmer sea surface temperature is causing increased mixing resulting in a deeper mix layer. The well-mixed layer is deeper in case C1 through t = 126 h (not shown). After t = 126 h, the well-mixed layer appears to be approximately the same height, but for case C it is cooler. The potential temperature gradient across the front is larger in the case C. The along-front wind velocity is less, and the convergence at the surface is less resulting in less ascending motion for case C1. With the warmer sea surface temperature cooling near the surface is reduced so the cold pool behind the front is warmer than in case C. Because the cold pool is cooler in case C, the temperature gradient within the inversion at the top of the boundary layer is stronger.

Maximum along-front wind velocity is less in case C1 than case C at all times (Figure 12) this is due to increase vertical mixing as indicated by higher K_m values until t = 80 h (Figure 13). The frontal scale for case C1 is larger than case C at after t = 80 h, but by t = 168 h both simulations have the same D value. The additional heat flux in case C1 initially slows frontogenesis, but eventually both fronts acheive the same small scale.

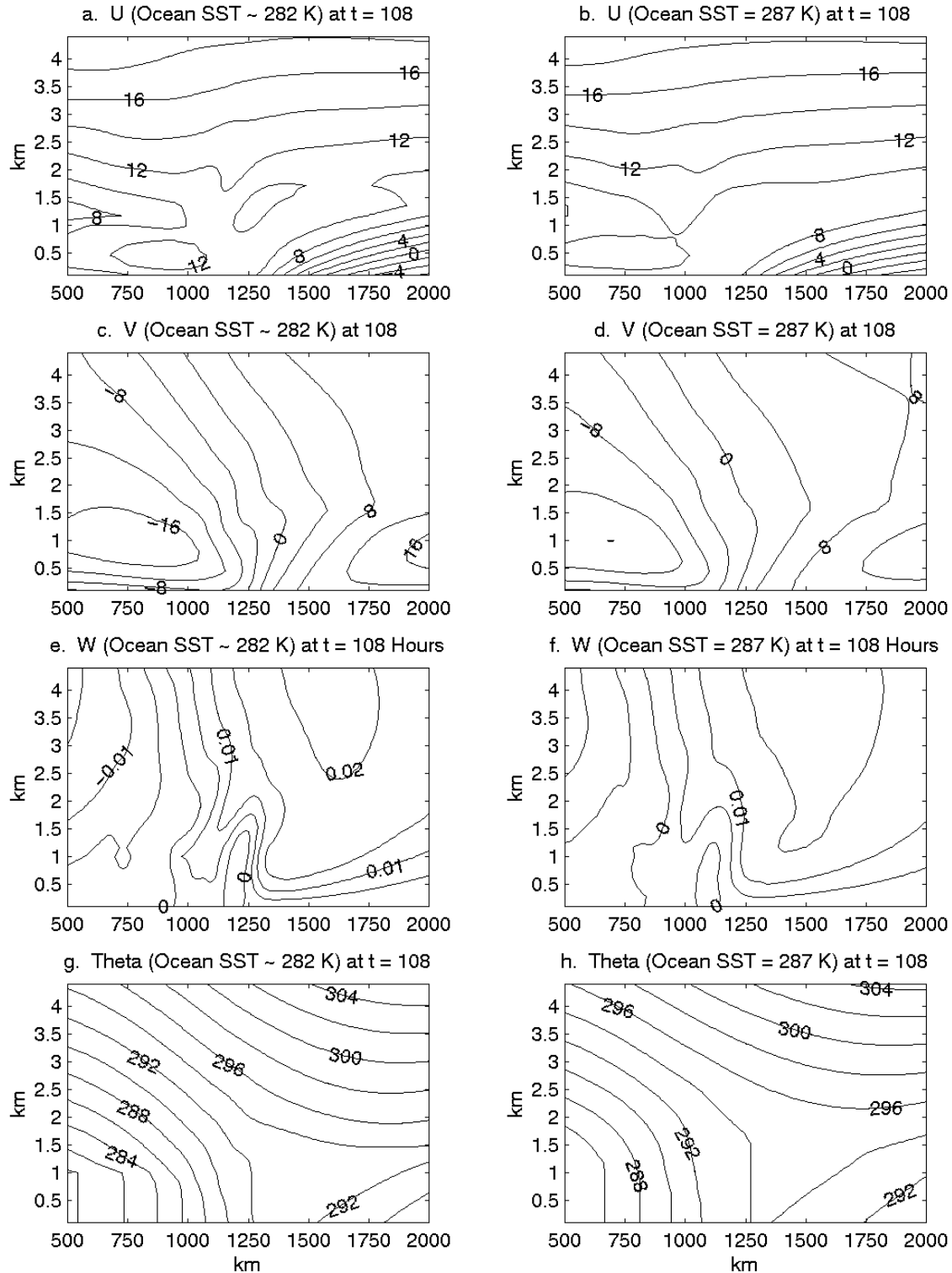Figure 19.   Frontal solutions for cases C and C1 for t = 108 h: (a) U (m s^{-1}) for ocean simulation SST ~ 282 K (case C); (b) U (m s^{-1}) for ocean simulation SST = 287 K (case C1); (c) V (m s^{-1}) for case C; (d) V (m s^{-1}) for case C1; (e) W (m s^{-1}) for case C; (f) W (m s^{-1}) for case C1; (g) Theta (K) for case C; (h) Theta (K) for case C1.

37

THIS PAGE INTENTIONALLY LEFT BLANK

V. CONCLUSIONS

The numerical simulations conducted in this study indicate that the PBL plays an important role in maritime frontogenesis. The effects in the inviscid simulation are consistent with those found in other studies. Specifically, it produced intense fronts with strong convergence and vorticity. Frontogenetic forcing was due primarily to shearing deformation. Using higher horizontal resolution, smaller scale fronts are achieved.

Relative to the frictionless results, the PBL simulations produced more realistic frontogenesis. Surface heat and momentum fluxes combined with turbulent mixing of heat promoted the development of a deep, well-mixed layer. In the PBL simulations the fronts do not tilt in the vertical over the lowest portion of the atmosphere. This structure is consistent with observations of fronts over the northeast Pacific Ocean (Bond and Fleagle 1985).

Frontogenesis is extremely dependent on the parameterization of the planetary boundary layer. Specifically, surface roughness lengths. During the land simulation, surface roughness length is fixed at 0.4 m and a well-mixed surface layer forms immediately. Frontogenesis is extremely slow and weakened during the land simulation. This agrees with cases treated by Keyser and Anthes (1982) and Peng *et al*. (2001). During the ocean simulations where surface roughness lengths are calculated and range from 0.001-0.002 m, the well-mixed layer takes longer to form. The addition of surface momentum flux clearly produces a well-mixed surface layer, reduces the along-front velocity and reduces the growth of the baroclinic wave. It takes longer for the frontogenesis to begin and for the PBL front to develop.

The addition of surface fluxes is not enough to properly simulate frontogenesis. Planetary boundary layer diffusion is also necessary. In the inviscid case rapid frontogenesis continues because the north-south temperature gradient does not change. In the simulation with small PBL diffusion, surface drag reduces the near surface wind and the convergence in the boundary layer, but the front still continues to grow and produces unrealistic along-front velocities by 5.5 days.

Air-sea temperature differences determine the depth of the well-mixed layer. In both ocean simulations as the cold air is brought in from the north, the air becomes colder than the water. This temperature difference is increased for simulation C1 which has a 5° higher water temperature. Turbulence and mixing are increased with the larger upward heat flux associated with the warmer seawater in simulation C1 as seen in the higher planetary boundary layer diffusion values.

Frontogenetic forcing in all simulations is due primarily to shearing deformation initially. As the wave grows in amplitude, convergence contributes more to frontogenesis than shear. Other terms in the frontogenetic equation become important in the PBL simulations since surface momentum flux, surface heat flux and PBL diffusion have been added.

Smaller scale fronts were achieved in the ocean simulations than in the land simulation agreeing with observational studies (Bond and Fleagle 1985; Fleagle *et al.* 1988; Chien *et al.* 2001). Increased horizontal resolution produced even smaller scale fronts.

In the future, the addition of other surface layer elements including moisture should be investigated and higher resolution simulations should be conducted to try and achieve smaller scale frontal features. Condensation enhances surface convergence locally by warming the column through the release of the latent heat. The impact of this associated latent heat release on frontogenesis can be important. Latent heat release, due to the lifting of moist unstable air in the lower levels of the troposphere, appeared to be critical to frontogenesis. Depending on the level of convection and corresponding latent heat release, the vertical motion profiles will be altered and therefore the tilting term of the frontogenetic equation will be changed. In addition to areas of increased ascent within the clouds there will be areas of descent between clouds. The location of maximum cyclonic vorticity is dependent on the vertical motion distribution and therefore the distribution of convective heating. Condensation will also redistributing surface air upwards so that comparatively high θ_e air is located along the tropopause. Because the extent and level of condensation can vary significantly the over all effect on

the vertical motion field and heating make it difficult to hypothesize on whether the addition of moisture would be frontogenetic or frontolytic.

THIS PAGE INTENTIONALLY LEFT BLANK

LIST OF REFERENCES

Arakawa, A., and V.R. Lamb, 1977: Computational design of the basic dynamical processes of the UCLA general circulation model. *Methods in Computational Physics*, **17**, Academic Press, 174-264.

Blackadar, A. K., 1979: High resolution models of the planetary boundary layer. *Advances in Environmental Science and Eng.*, **1**, J. R. Pfafflin and E. N. Ziegler, eds., Gordon and Breach, 50-85.

Bond, N. A., and R. G. Fleagle, 1985: Structure of a cold front over the ocean. *Quart. J. Roy. Meteor. Soc.*, **111,** 739-759.

Businger, J.A., J.C. Wyngaard, Y. Izumi, E.F. Bradley, 1971: Flux-profile relationships in the atmospheric surface layer. *J. Atmos. Sci.*: **28**, 181–189.

Chien, F., C. F. Mass, P. J. Neiman, 2001: An observational and numerical study of an intense landfalling cold front along the northwest coast of the United States during COAST IOP 2. *Mon. Wea. Rev.*, **129**, 934–955.

Dyer, A. J., 1974: A review of flux-profile relationships. *Bound.-Layer Meteor.*, **7,** 363-372.

Ellison, T. H., and J. S. Turner, 1959: Turbulent entrainment in stratified flows. *J. Fluid Mech.*, **6**, 423-448.

Estoque, M. A. and C. M. Bhumralkar, 1970: A method for solving the planetary boundary layer equations. *Bound.-Layer Meteor.*, 1**,** 169-174.

Fichtl, G. H. and G. E. McVehil, 1970: Longitudinal and lateral spectra of turbulence in the atmospheric boundary layer at Kennedy Space Center, *J. Appl. Meteor.,* **9**, 51-63.

Fleagle, R.G., N.A. Bond, and W.A. Nuss, 1988: Atmosphere-ocean interaction in mid-latitude storms. *J. Meteor. Atmos. Phys.*, **38***,* 50-63.

Garratt, J.R., 1977: Review of drag coefficients over oceans and continents. *Mon. Wea. Rev.*: **105**, 915–929.

Garratt, J.R., 1980: Surface influence upon vertical profiles in the atmospheric near-surface layer. *Quart. J. Roy. Meteor. Soc.*, **106,** 803-819.

Garrett, J. R., 1992: The atmospheric boundary layer, J. T. Houghton, M. J. Rycroft, and A. J. Dessler, eds., Cambridge University Press, 100-101.

Hicks, B.B., 1970: The measurement of atmospheric fluxes near the surface: a generalized approach. *J. Appl. Meteor.*, **9**, 386–388.

Hodur, R. M., 1997: The Naval Research Laboratory's Coupled Ocean/Atmosphere Mesoscale Prediction System (COAMPS). *Mon. Wea. Rev*., **125**, 1414-1430.

Högstrom, U., 1988: Non-dimensional wind and temperature profiles in the atmospheric surface layer: A re-evaluation. *Bound.-Layer Meteor.*, **42,** 55-78.

Holtslag A. A. M. and De Bruin, H. A. R. , 1988: Applied modeling of the night-time surface energy balance over land. *J. Appl. Meteor*., **27**, 689-704.

Keyser, D. and Anthes, R.A., 1982: The influence of planetary boundary layer physics on frontal structure in the Hoskins-Bretherton deformation model. *J. Atmos. Sci.*, **39**, 1783-1802.

Lee, R. L. and D. B. Olfe, 1974: Numerical calculations of temperature profiles over an urban heat island, *Bound.-Layer Meteor.*, **7,** 39-52.

Louis, J. F., 1979: A parametric model of vertical eddy fluxes in the atmosphere. *Bound.-Layer Meteor.,* **17,** 187-202.

Mellor, G. L., T. Yamada, 1974: A Hierarchy of Turbulence Closure Models for Planetary Boundary Layers. *J. Atmos. Sci.*: **31**, 1791–1806.

Monin, A. S. and A. M. Obukhov, 1954: Basic laws of turbulent mixing in the atmosphere near the ground, *Tr. Akad. Nauk SSSR Geofiz. Inst.,* **24**, 163-187.

Ogura, Y. and N. A. Phillips, 1962: Scale analysis of deep and shallow convection in the atmosphere. *J. Atmos. Sci.*: **19**, 173–179.

Paulson, C. A., 1970: The mathematical representation of wind speed and temperature profiles in the unstable atmospheric surface layer. *J. Appl. Meteorol.*, **9,** 857-861.

Peng, M. S., J. H. Powell, R. T. Williams, B. Jeng, 2001: Boundary Layer Effects on Fronts over Topography. *J. Atmos. Sci.*, **58**, 2222–2239.

Shieh, C. M. and W. J. Moroz, 1975: Mathematical modeling of lake breeze, *Atmos. Envir.,* **9**, 575-586.

Thompson, W. T., R. T. Williams, 1997: Numerical simulations of maritime frontogenesis. *J. Atmos. Sci.*, **54**, 314–331.

Thompson, W. T., M. Shapiro, and N. A. Bond, 2000: Interaction of a stable marine boundary layer with a low-level jet. *14th Symposium on Boundary Layer and Turbulence,* Aspen, CO, 7-11 August 2000.

Torrance, K. E. and J. S. W. Shum, 1976: Time varying energy consumption as a factor in urban climate, *Atmos. Envir.,* **10**, 329-337.

Williams, R. T., 1967: Atmospheric frontogenesis: a numerical experiment. *J. Atmos. Sci.*, **24**, 627-641.

Williams, R.T., 1974: Numerical simulation of steady-state fronts. *J. Atmos. Sci.*, **31**, 1286-1296.

Williams, R.T., L. C. Chou, C. J. Cornelius, 1981: Effects of condensation and surface motion on the structure of steady-state fronts. *J.Atmos. Sci.*: **38**, 2365–2376.

Williams, R. T., M. S. Peng, D. A. Zankofski, 1992: Effects of topography on fronts. *J. Atmos. Sci.*: **49**, 287–305.

THIS PAGE INTENTIONALLY LEFT BLANK

INITIAL DISTRIBUTION LIST

1. Defense Technical Information Center
    Ft. Belvoir, Virginia

2. Dudley Knox Library
    Naval Postgraduate School
    Monterey, California

3. Chairman, Code MR
    Meteorology Department
    Naval Postgraduate School
    Monterey, California

4. Prof. R. T. Williams
    Meteorology Department
    Naval Postgraduate School
    Monterey, California

5. Dr. W. A. Nuss
    Meteorology Department
    Naval Postgraduate School
    Monterey, California

6. Dr. D. K. Miller
    Meteorology Department
    Naval Postgraduate School
    Monterey, California

7. Dr. M. S. Peng
    Naval Research Laboratory - Monterey
    7 Grace Hopper Avenue
    Monterey, California 93943-5502

8. Dr. W. T. Thompson
    Naval Research Laboratory - Monterey
    7 Grace Hopper Avenue
    Monterey, California 93943-5502

9. LCDR C. M. McDougall
    3345 Ross Lane
    East Jordan, Michigan 49727